NASA/TP–20220015152

Optimization Approach for Wind Tunnel Fan Blade Strain Gage Correlation with Test Fixture Unknowns

Brian H. Mason and Andrew E. Lovejoy
Langley Research Center, Hampton, Virginia

October 2022

NASA STI Program Report Series

Since its founding, NASA has been dedicated to the advancement of aeronautics and space science. The NASA scientific and technical information (STI) program plays a key part in helping NASA maintain this important role.

The NASA STI program operates under the auspices of the Agency Chief Information Officer. It collects, organizes, provides for archiving, and disseminates NASA's STI. The NASA STI program provides access to the NTRS Registered and its public interface, the NASA Technical Reports Server, thus providing one of the largest collections of aeronautical and space science STI in the world. Results are published in both non-NASA channels and by NASA in the NASA STI Report Series, which includes the following report types:

- TECHNICAL PUBLICATION. Reports of completed research or a major significant phase of research that present the results of NASA Programs and include extensive data or theoretical analysis. Includes compilations of significant scientific and technical data and information deemed to be of continuing reference value. NASA counterpart of peer-reviewed formal professional papers but has less stringent limitations on manuscript length and extent of graphic presentations.

- TECHNICAL MEMORANDUM. Scientific and technical findings that are preliminary or of specialized interest, e.g., quick release reports, working papers, and bibliographies that contain minimal annotation. Does not contain extensive analysis.

- CONTRACTOR REPORT. Scientific and technical findings by NASA-sponsored contractors and grantees.

- CONFERENCE PUBLICATION. Collected papers from scientific and technical conferences, symposia, seminars, or other meetings sponsored or co-sponsored by NASA.

- SPECIAL PUBLICATION. Scientific, technical, or historical information from NASA programs, projects, and missions, often concerned with subjects having substantial public interest.

- TECHNICAL TRANSLATION. English-language translations of foreign scientific and technical material pertinent to NASA's mission.

Specialized services also include organizing and publishing research results, distributing specialized research announcements and feeds, providing information desk and personal search support, and enabling data exchange services.

For more information about the NASA STI program, see the following:

- Access the NASA STI program home page at http://www.sti.nasa.gov

- Help desk contact information:

https://www.sti.nasa.gov/sti-contact-form/
and select the "General" help request type.

NASA/TP–20220015152

Optimization Approach for Wind Tunnel Fan Blade Strain Gage Correlation with Test Fixture Unknowns

Brian H. Mason and Andrew E. Lovejoy
Langley Research Center, Hampton, Virginia

National Aeronautics and
Space Administration

Langley Research Center
Hampton, Virginia 23681-2199

October 2022

Available from:

NASA STI Program / Mail Stop 148
NASA Langley Research Center
Hampton, VA 23681-2199
Fax: 757-864-6500

Optimization Approach for Wind Tunnel Fan Blade Strain Gage Correlation with Test Fixture Unknowns

Brian H. Mason and Andrew E. Lovejoy
NASA Langley Research Center, Hampton, VA 23681-2199

NASA has a significant maintenance challenge with the aging wind tunnel infrastructure across the Agency. Some wind tunnel fan blades, such as those in the National Transonic Facility at NASA Langley Research Center, have been in use for far longer than their planned 10-year lifetime. No detailed analytical models of the fan blades from their initial fabrication were created. To support the fabrication of either new, nominally identical fan blades or newly designed fan blades, accurate analytical models of the existing fan blades are necessary to demonstrate an understanding of the capabilities of the existing fan blades. Additionally, the existing documentation of the testing of the existing fan blades has gaps. In this report, a process for improving test-analysis correlation for these wind tunnel fan blades is discussed. This process involved a detailed study of unknown parameters in test fixture parameters from the old and incomplete test documentation. To improve correlation, these unknown parameters were used as design variables in an optimization study to minimize the error between test data and computed structural responses. Legacy strain gage data from tests conducted in 1981 were compared with results from a finite element model created in 2019. The use of test data from 1981 was necessary because none of the existing fan blades could be spared for use in destructive structural testing. While this process was demonstrated for wind tunnel fan blades, this process could be utilized for evaluating unknowns in test fixtures for other structural test configurations.

I. Introduction

The Aerosciences Evaluation and Test Capabilities (AETC) portfolio office is charged with setting the strategic direction for aeronautics research facilities at NASA. The aging wind tunnel infrastructure at NASA poses a challenge to this office. To overcome this challenge, AETC makes targeted investments in maintaining and improving these research facilities. Among these wind tunnel research facilities is the National Transonic Facility (NTF) [1] at the NASA Langley Research Center (LaRC). Accumulation of fatigue damage to the fan blades and fan blade loss due to impact damage are of particular concern to the NTF wind tunnel. Fabrication of replacement fan blades for NTF may soon be required by AETC. Unfortunately, new fan blades have not been built for over thirty years, so two studies were initiated as a precursor to development of plans for fan blade fabrication. The two studies were Preparing Researchers to Evaluate and Develop Impact–Driven Collaborative Technologies (PREDICT) in 2018 [2–5] and a follow-on activity [6] from 2019 to the present. In this report, development of geometric and structural models for the two studies is described. A study of the legacy test procedures for the original fan blades is also presented, and correlation between test data and analysis of the new structural models is performed using optimization methods and an evaluation of unknowns in the legacy test fixtures.

A. Motivation and Background

The NTF [1] is a wind tunnel at LaRC that became operational in 1984. The NTF was designed for testing of aerospace vehicles ranging from subsonic to low supersonic speeds with high Reynolds numbers at temperatures from -256°F to +151°F. The NTF is driven by a set of 25 wind tunnel fan blades in the fan section such as the one illustrated in Figure 1a. Each fan blade contains a hollow glass-epoxy composite structure that is continuous from the fan blade tip (in the airfoil section) to the pin-wrap connection at the hub. The middle of the fan blade is enclosed in a box-like sandwich structure, called the platform section (including the platform, fairings, and channels as shown in Figure 1a). The platform section holds a fan blade circumferentially on the 12-ft-diameter hub and forms the interior aerodynamic surface of the fan section, as shown in Figure 1b.

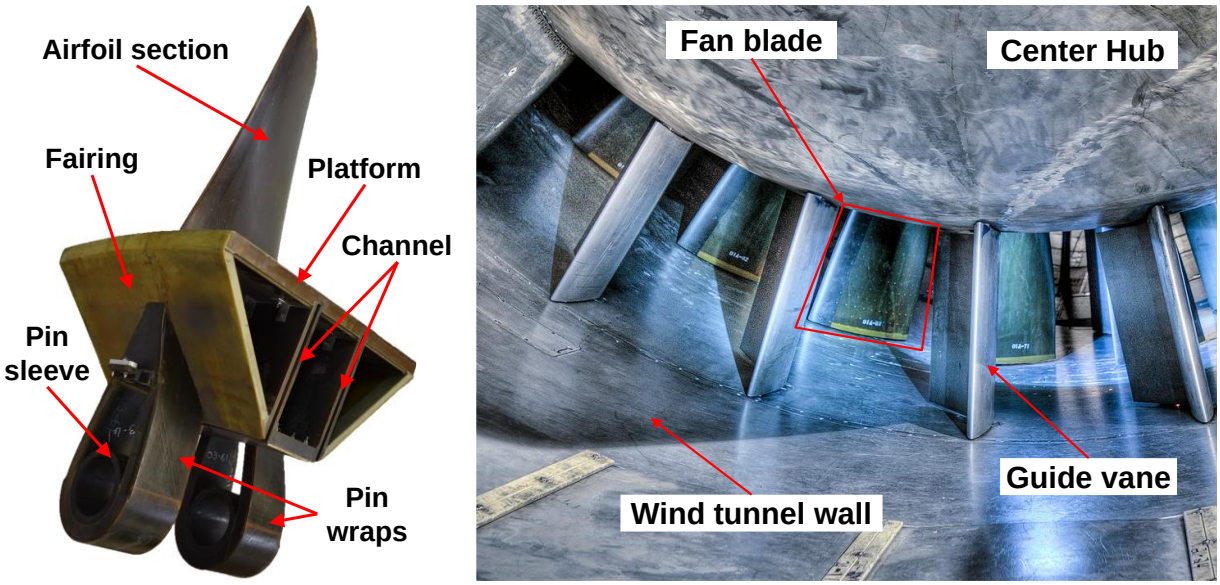

a) Fan blade outside tunnel **b) Fan blade inside tunnel drive section**

Figure 1. NTF wind tunnel fan blade.

Three full sets of fan blades have been fabricated for NTF since 1981. The first set of fan blades was destroyed in an impact incident in 1989 [1, 7]. A second set of fan blades was manufactured by NASA and installed in the tunnel in August of 1989. A third set of fan blades was fabricated by Dynamic Engineering Incorporated in 1991. Over the last thirty years, several more fan blades have been damaged beyond repair due to impact incidents. At present, one full set is in operation and a partial spare set of 10 fan blades exists, which presents an operational risk. If a future incident results in a substantial loss of fan blades, the tunnel may face a long period of inoperability. Because the last set of NTF fan blades was fabricated in 1991, NASA personnel are investigating advances in fabrication methodologies that have the potential to significantly reduce the costly downtime associated with potential future fan blade repairs or replacement, among other benefits, such as reduced manufacturing costs, improved performance, lower weight, etc.

The first project to investigate the steps necessary to fabricate new fan blades was the PREDICT study. The project was carried out over the summer of 2018 by a small team working at the Integrated Structural Assembly of Advanced Composites (ISAAC) facility at LaRC [8]. The goal of the PREDICT study was to perform an initial assessment of the use of automated fiber placement (AFP) and other advanced manufacturing methods to fabricate fan blades for NTF and other agency wind tunnels. During the PREDICT study [2–5], a composite part with a representative contoured wind tunnel fan blade shape was successfully fabricated using AFP with the ISAAC robotic system. A photograph of the ISAAC robotic system is shown in Figure 2.

In the fall of 2018, AETC initiated a follow-on to the PREDICT study to further examine wind tunnel fan blade redesign, fabrication, and replacement. The goal of this fan blade study was to evaluate the design requirements and limitations of the original NTF wind tunnel fan blades, and to recommend the best approach to fabricate new fan blades. The two approaches under consideration were: 1) to fabricate fan blades that were nominally identical to the legacy fan blades, or 2) to develop enhanced fan blades to replace the current set. Enhanced fan blades built using ISAAC offer the potential of reduced weight, reduced cost, and reduced effort to initiate fabrication. Detailed structural models of the current NTF wind tunnel fan blades are required for evaluation of the fan blade performance and to support any new fan blade design.

In the fall of 2019, a study was performed to correlate strain gage results from a series of tests in 1981 with a newly created finite element model (FEM) [6]. Obtaining detailed geometry and material information for the model described in this report was challenging and poor definition of the conditions of 1981 testing hindered correlation of results between the new FEM and the old test data. The optimization process developed in conjunction with a review of the unknowns in modeling the test fixtures to improve the test-analysis correlation is described in this report.

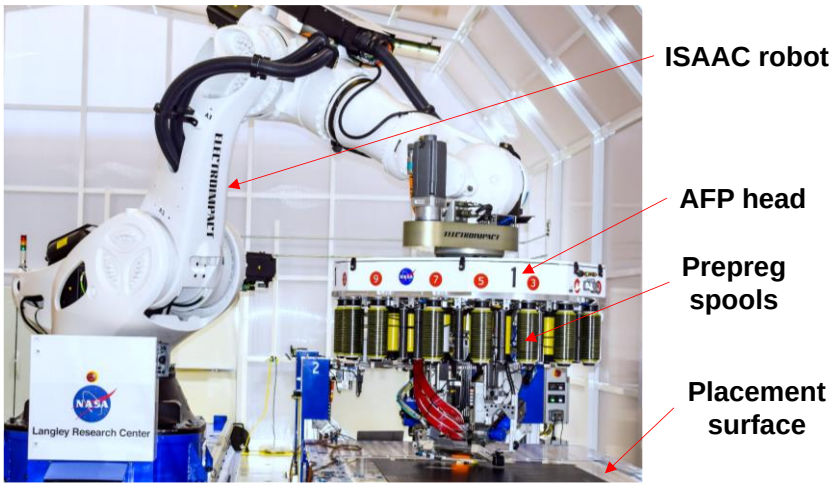

Figure 2. Advanced manufacturing using AFP at the ISAAC facility.

B. Purpose and Content

In this report, a process for improving test-analysis correlation for wind tunnel fan blades is discussed. This process involved a detailed study of unknowns in test fixture parameters from old, incomplete test documentation. To improve correlation, these unknown parameters were used as design variables in an optimization study to minimize the error between test data and computed structural responses. Whenever possible, characterization of the fixture(s) as well as the test article using measurement techniques such as digital image correlation (DIC) [9,10] is the best approach; however, when that is not possible, the process presented herein for wind tunnel fan blades can be utilized for evaluating unknowns in test fixtures for other structural test configurations.

Correlation of new numerical structural models with old experimental data was desired to understand the structural performance of the legacy fan blades. Accurate structural models are necessary for development of manufacturing processes and for recertification of newly fabricated fan blades. Therefore, use of old test data for validating the FEM was desired because none of the existing fan blades could be spared for use in destructive structural testing.

The report is organized as follows. In section II, development of the wind tunnel fan blade geometry from legacy documentation and examination of a physical fan blade is reviewed. In section III, material properties and fabrication of the fan blade is discussed. Next, the testing program used to certify the original fan blades is presented in section IV. Structural modeling and analysis of the fan blade under wind tunnel operating conditions are discussed in section V. The optimization process and the unknown test fixture parameters used in improving the test-analysis correlation are summarized in section VI. Results from optimization studies used to improve the test- analysis correlation for the centrifugal and aerodynamic loading test cases are presented in sections VII and VIII, respectively. Test-analysis correlation for the two combined loading test cases was improved using the optimized test fixture parameters from sections VII and VIII, as shown in section IX. The report ends with a summary and discussion of results in section X and with concluding remarks in section XI.

II. Development of NTF Wind Tunnel Fan Blade Geometry

The original NTF wind tunnel fan blades were fabricated in the early 1980s in a complex process involving several E-glass/epoxy prepreg layups, multiple cure cycles, assembly of numerous subcomponents, and many inspection and machining operations. Approximately eight thousand pages of legacy documentation exist for the design of the original NTF wind tunnel fan blades. Several sets of drawings of the original fan blades were extracted from the legacy documentation, but no computer-aided design (CAD) geometry of the fan blades existed prior to the 2019 study [6]. In the 2019 study, CAD geometry representative of a fan blade was created based on legacy data to be used for structural modeling, tool development, and potentially for inspection and validation of newly manufactured fan blades.

Herein, the complete fan blade assembly shown in Figure 1a is referred to as the fan blade, while the platform, channel, and fairings are referred to as the platform section. The fan blade coordinate system is shown for a CAD model of the fan blade in Figure 3. The root-to-tip, or centrifugal, direction is the Z-direction, and the chord, or pin, direction is the X-direction. The Y-direction represents depth and is normal to the centrifugal and pin directions. The platform section is shown in green in Figure 3a, but the platform section is removed from Figure 3b for better visualization of the other sections. In Figure 3b, the blue section (referred to as the root section) includes the pin-wraps and pin sleeve where the fan blade is attached to the wind tunnel hub. The airfoil section of the fan blade is colored red in the figure and extends above the platform and into the airflow.

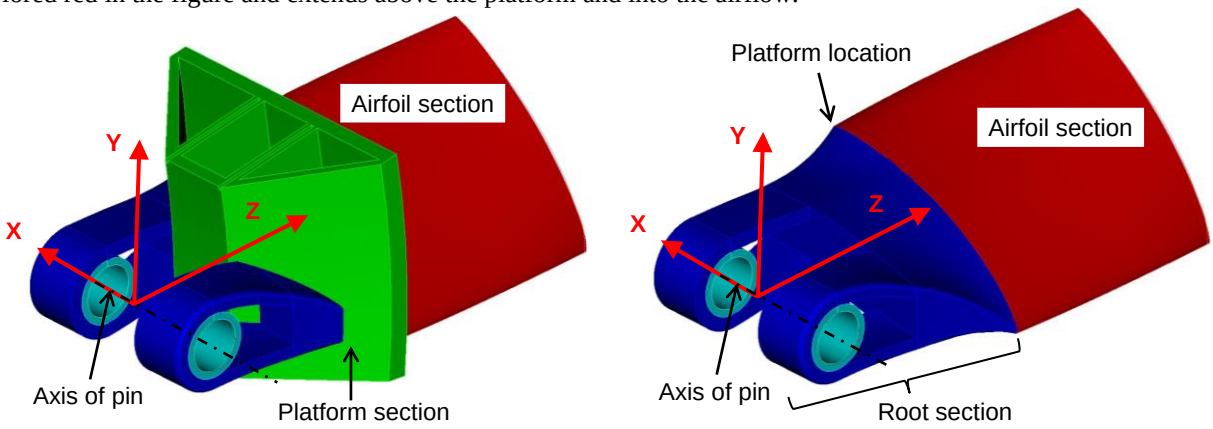

a) Isometric view **b) Isometric view with platform section removed**

Figure 3. CAD of NTF wind tunnel fan blade with coordinate system.

Drawings of the fan blade with the platform section removed are shown in Figure 4. The fan blade is 51.8-in. long and 19.2-in. wide at the pin location. As shown in Figure 4a, the main structure within the fan blade is a spar. The upper and lower covers of the spar were fabricated as continuous sheets of fiberglass fabric wrapping around the pin sleeve. In the airfoil section, the upper and lower covers of the spar are wrapped around a mold to form a hollow box structure, as shown in Figures 4b and 4c. The leading and trailing edges of the airfoil section were not hollow but were filled with syntactic foam. The spar ends a short distance from the fan blade tip, which is frangible. As seen in Figure 4d, at the platform location, the airfoil cross-section is twisted 26.9° around the Z-axis. At the fan blade tip, the twist angle of the airfoil cross-section is 47.4°.

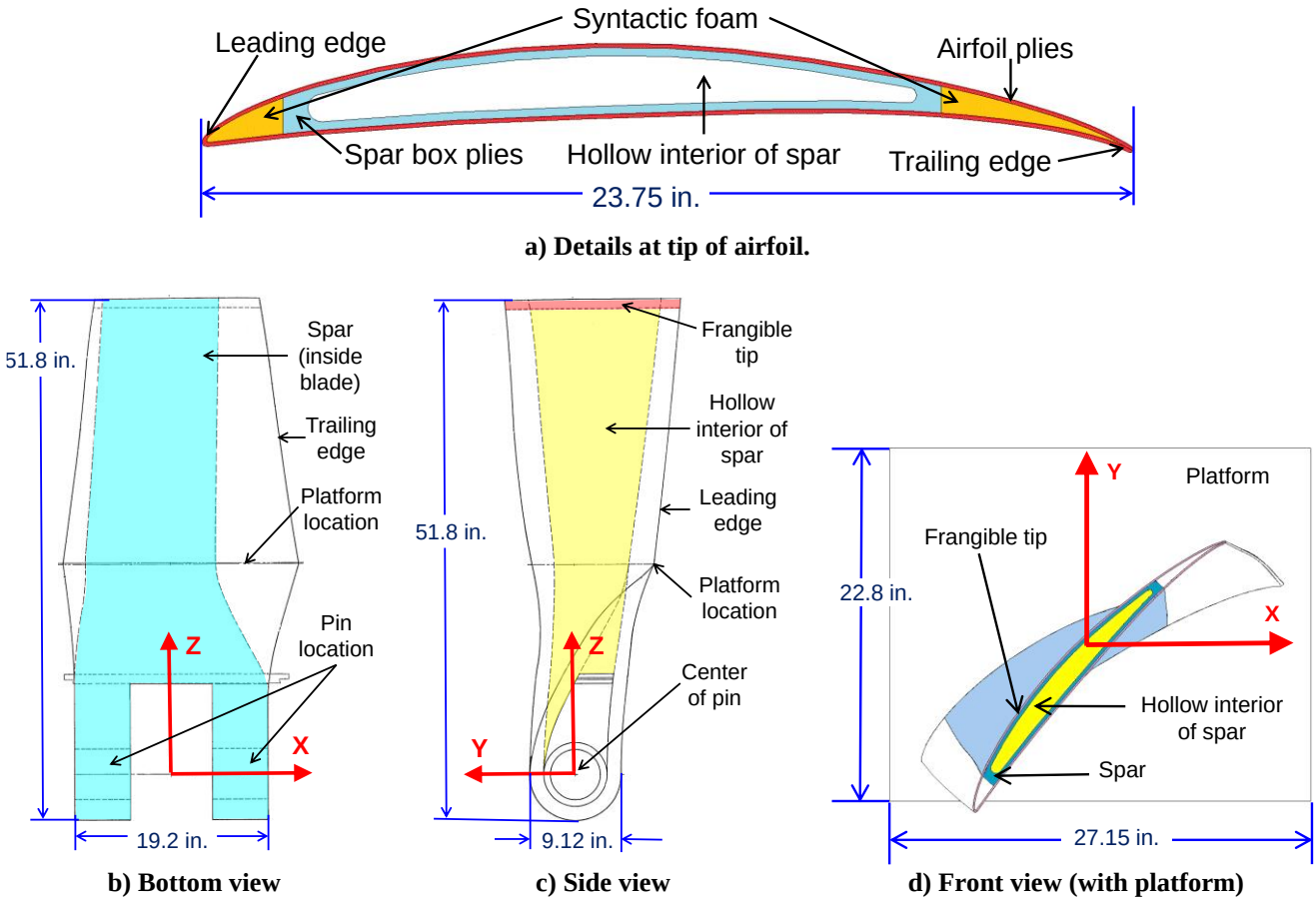

a) Details at tip of airfoil.

b) Bottom view **c) Side view** **d) Front view (with platform)**

Figure 4. Drawings of NTF wind tunnel fan blade with dimensions.

During a review of legacy documentation in the 2019 study [6], coordinates defining the final shape of the fan blade structure were located. These coordinates consisted of data at twenty cross sections, which were used as input to a numerical control machining tool. A subset of the dimensions was extracted from the machine tool coordinates and used to generate CAD of the airfoil and root sections of the fan blade. Data for five airfoil sections, spaced evenly from the platform station to the airfoil tip, are plotted in Figure 5. The chord length varies from 26 in. at the root (platform station) to 23.75 in. at the tip, and the thickness-to-cord ratio varies from 10% at the root to 6% at the tip. The airfoil sections do not match standard airfoil sections in the National Advisory Committee for Aeronautics (NACA) database.

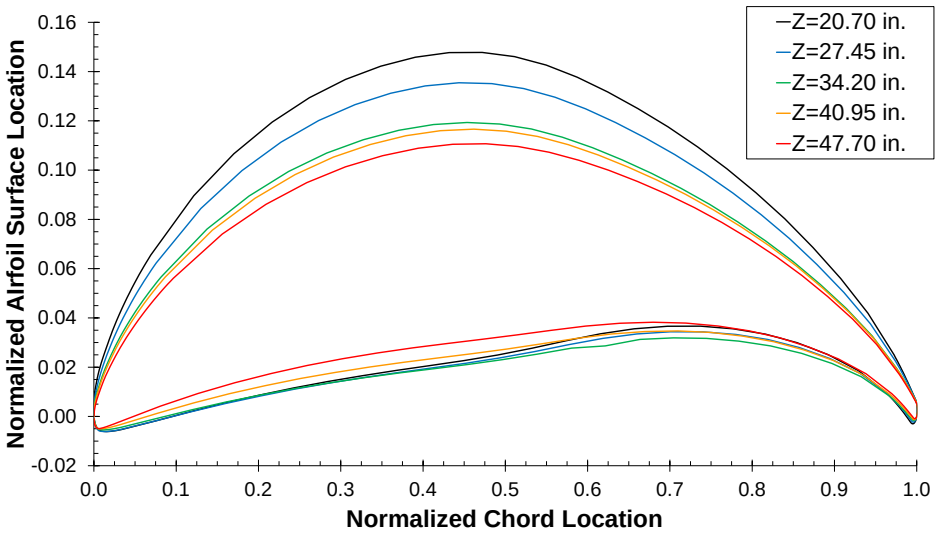

Figure 5. Airfoil dimensions for the NTF fan blade.

Dimensioned drawings of the platform and fairing were not located in the legacy documentation, so measurement of a spare fan blade was performed to obtain dimensions of the platform and fairing to help construct the CAD model. As each fan blade is one in a set of 25 around the fan center hub, the platform and fairing fit within a 14.4° arc, and this measurement was used to help define the geometry of the platform section.

As previously mentioned, the machining tool data included coordinates at twenty cross sections prior to the addition of the platform and fairing. Data from nine of these cross sections (4 in the root and 5 in the airfoil) were digitized and imported into the Cubit [11] geometry modeling tool to develop a complete surface of the outside of the airfoil. It was not clear whether the documents used for defining the dimensions of the CAD geometry represented the final design or some intermediate step in the fabrication process. Due to this uncertainty with the dimensions, a laser scan was conducted using a Nikon LC60Dx digital coordinate measuring machine (CMM) scanner [12] to measure the as-manufactured geometry of one of the current fan blades. The scan data is overlaid on the CAD geometry in Figure 6. In Figure 6, the scanned data is shown as yellow, and the CAD geometry is shown in red, blue, and green. Holes in the yellow scanned data indicates regions in which the CAD geometry is outside the scanned data from the reader's point of view. Numerical data for the accuracy of the CAD geometry with respect to the original scan data is not available. However, recently, additional laser scans of a fan blade were conducted using a Creaform Metrascan system [13]. For these new scans, the average and maximum error between the scanned point cloud and the airfoil section geometry was 0.007 in. and 0.220 in., respectively, which was considered an adequate level of geometric accuracy.

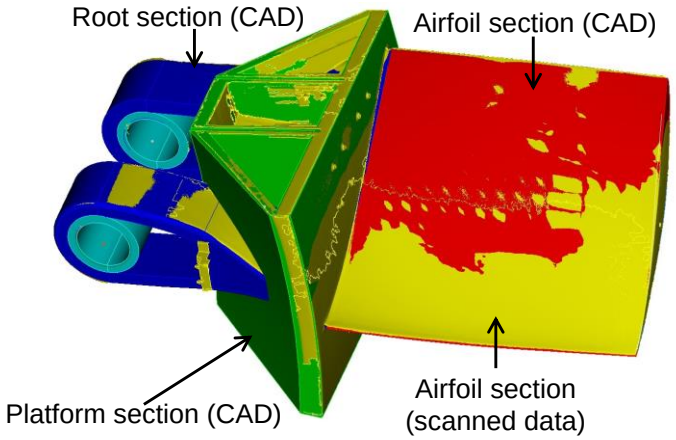

Figure 6. CAD geometry of the NTF fan blade with overlaid scan data.

III. Material Properties of NTF Wind Tunnel Fan Blade

The original NTF wind tunnel fan blade was fabricated in a complex process involving numerous steps. The three major steps were fabrication of the internal fan blade spar (shown in blue in Figure 4a), fabrication of the airfoil outer mold line (OML), and attachment of the platform and fairing. The fan blade was fabricated from two types of E-glass fabric/epoxy with material properties [14] given in Table 1. The ply layups of the fan blade contained a large number of thickness changes, or ply drops. The plies in the fan blade were a mixture of 0° 7576 fabric and 0° and ±30° 7781 fabric. The ply stacking sequences are too detailed to present in this report; so, the number of plies in the spar and airfoil sections is plotted against the centrifugal stations in Figure 7. The spar was 100-plies thick at the fan-blade root and pin location, tapering down to 23 plies at the airfoil tip through numerous ply drops. Similarly, the airfoil section encasing the fan blade tapered from 44 plies in the fan blade root to 7 plies at the tip. Five additional plies were placed on the outside of the fan blade, bringing the maximum thickness of the fan blade to 149 plies at the root. The platform, fairing, and channel were fabricated as a sandwich structure consisting of ±45° 7781 fabric with a variable number of plies. The exact properties of the sandwich core are unknown; so, properties for a generic honeycomb core were used.

Table 1. Material properties of fiberglass in the NTF wind tunnel fan blade.

Property	7576 EF-2 E-Glass Cloth [14]	7781 EF-2 E-Glass Cloth [14]	Generic Honeycomb Core
Nominal Ply Thickness, in.	0.011	0.009	0.66 – 0.90
Elastic Modulus – Longitudinal, Msi	5.750	3.800	0.001
Elastic Modulus – Transverse, Msi	2.640	3.840	0.001
Shear Modulus, Msi	0.990	0.750	0.075
Poisson's Ratio	0.2570	0.1440	0.4500
Tensile Strength – Longitudinal, ksi	105.900	57.023	N/A
Tensile Strength – Transverse, ksi	10.053	43.582	N/A
Compressive Strength – Longitudinal, ksi	-100.337	-54.992	N/A
Compressive Strength – Transverse, ksi	-10.053	-43.582	N/A
Shear Strength, ksi	11.062	11.911	N/A

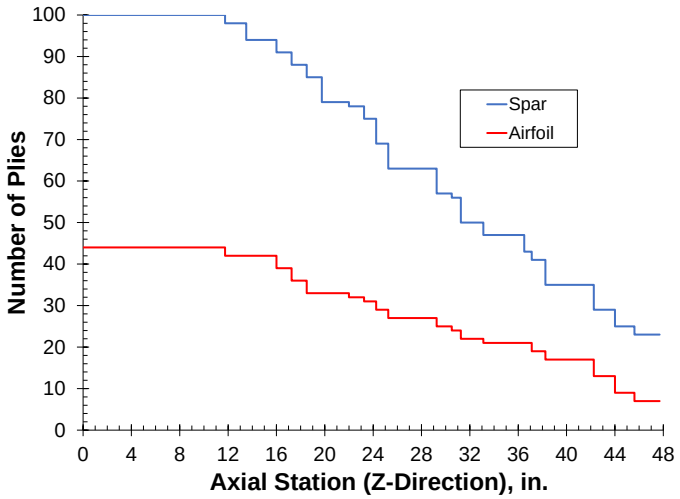

Figure 7. Thickness distribution for wind tunnel fan blade.

IV. Test Conditions

Structural and thermal testing was performed to certify the original NTF wind tunnel fan blades. Among these tests were quasi-static loading, natural frequency, centrifugal loading, fatigue loading, and temperature cycling. Legacy documentation was available for three sets of tests: quasi-static and fatigue loading tests performed at Fort Eustis Army Base in Newport News, Virginia [15], centrifugal loading tests performed at Wright Patterson Air Force Base (WPAFB) in Dayton, Ohio [16], and vibrational testing at LaRC [17]. Strain gage data from the Fort Eustis tests are compared with analytical results in sections VII through IX. Strain gage data from WPAFB was deemed too limited and subject to too many unknowns to warrant further study.

Quasi-static and fatigue testing was performed at Fort Eustis February 2-5, 1981 [15]. The test setup is illustrated in Figures 8 and 9. As shown in Figure 8, the fan blade was mounted horizontally with the platform rotated approximately 45° from horizontal. In Figure 9a, the centrifugal load introduction structure is shown as a load bar and a set of trapezoidal metallic plates, which were attached to the fan blade with three bolts 6.2 in. from the tip of the fan blade. Because the loads were applied through the thinner airfoil section, the centrifugal loading was significantly lower than the operating loads experienced in the thicker pin-wrap section. According to Ref. [15], the X- and Y-locations of the applied load coincided with the center of gravity (CG) of the airfoil section, but these actual dimensions were not specified. As shown in Figure 9b, a plate called a guillotine was attached to the fan blade 13.2 in. from the fan blade tip, and a representative aerodynamic load was applied to this plate in a vertical direction. The load was applied at the center of pressure (CP) of the airfoil. The test documents did not specify the exact location of the CP, but another document [18] stated that the CP of each airfoil section was at 35% of the chord length of a given section. This chordwise location was used in the analytical model in the next section.

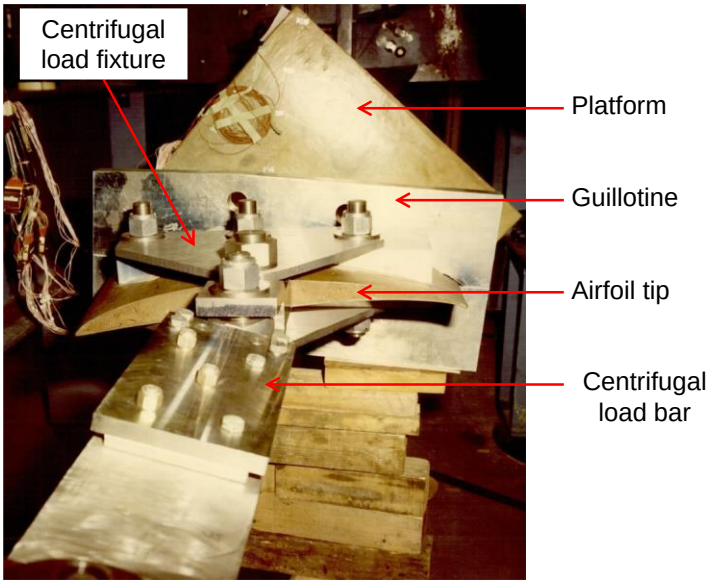

Figure 8. Photograph of quasi-static and fatigue test setup.

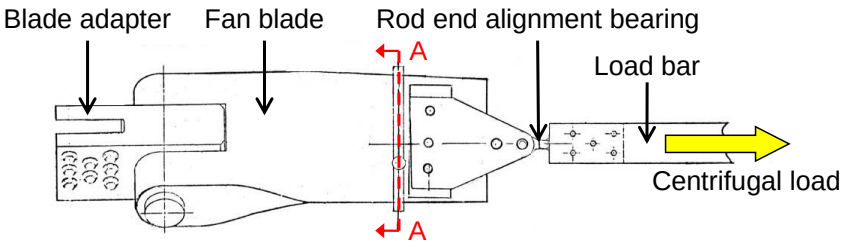

a) Test specimen with all load fixtures

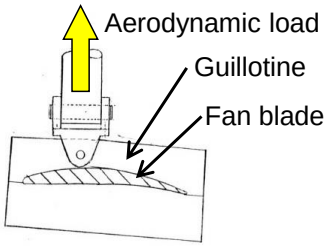

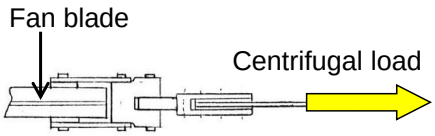

b) Aerodynamic load fixture, section A-A **c) Centrifugal load fixture**

Figure 9. Load fixtures for quasi-static and fatigue tests.

The test matrix is presented in Table 2. Because of the large amount of test data, only the subset of the test data highlighted in yellow (load cases 1, 2, 3, and 6) are discussed in the test-analysis correlation sections. The centrifugal loads represented the loads experienced by the airfoil section of the fan blade (above the platform) and were calculated from the mass of the airfoil (54 lbm) and the center of gravity of the airfoil (6.7 in. from the wing tip) at the given rotational speeds. The maximum aerodynamic loads were estimated to be 10.9 kips and 5.0 kips at 360 rpm and 600 rpm, respectively. In the combined load case, the aerodynamic load was increased to counter the transverse load generated by the centrifugal load applied in the test.

Table 2. Test matrix for static and fatigue tests at Fort Eustis in 1981.

Load Case	Test Type	Equivalent Rotational Speed, rpm	Maximum Centrifugal Load, kips	Maximum Aerodynamic Load, kips
1	Static (Centrifugal)	600	57.0	0.0
2	Static (Aerodynamic)	360	0.0	10.9
3	Static (Combined)	360	20.6	12.5
4	Fatigue (Combined)	360	20.6	12.5
5	Static (Combined)	360, same as 3	20.6	12.5
6	Static (Combined)	600	57.3	5.0
7	Fatigue (Combined)	600	57.3	5.0
8	Static (Combined)	600, same as 6	57.3	5.0
9	Static (Centrifugal)	600, same as 1	57.0	0.0
10	Static (Aerodynamic)	360, same as 2	0.0	10.9
11	Displacement	360	0.0	10.0

V. Finite Element Model

An FEM of the NTF wind tunnel fan blade was generated from the CAD geometry presented in Section II using the MSC/PATRAN [19] finite element modeling tool. Nonlinear static analyses were performed using the general-purpose finite element analysis (FEA) code Abaqus [20]. The FEM consisted of 18,818 composite shell (S4R quadrilateral and S3R triangular) elements and 17,848 nodes and is illustrated in Figure 10. The pin and pin sleeve in the root section were modeled together as an analytical rigid cylinder. Incorporation of the pin sleeve in the rigid pin was a modeling simplification, motivated by a lack of material data for the sleeve. The hub section at the bottom of the platform was also modeled with a rigid cylinder and two rigid rectangles to represent the sides of the hub. The Abaqus surface contact algorithm (with a friction coefficient of 0.3) was used to define the interaction between the rigid pin and the fan blade root. The centrifugal load fixture was represented by six rigid links between the fan blade and a free node representing the load application point. In Figure 10a, the complete FEM is illustrated, including the rigid pin, three rigid hub sections, and load application structures. In Figure 10b, the platform section is removed to show the airfoil and root sections. The shell elements at the leading edge (LE) and trailing edge (TE) have approximately one third the thickness of the middle section, which includes both the spar and the outer airfoil plies (the actual thickness values are shown in Figure 7). The rigid pin and hub are constrained in translational and rotational coordinates, and the contact algorithm is used to connect the fan blade structure to these rigid surfaces. No displacement constraints were applied to the aerodynamic or centrifugal load application nodes.

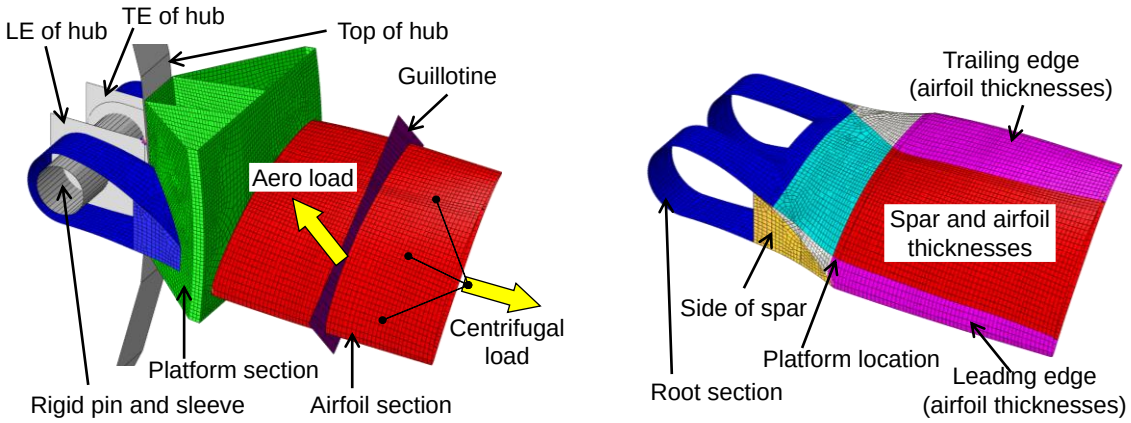

a) Complete model with loads **b) Model with platform and rigid bodies removed**

Figure 10. Finite element model of fan blade.

The mesh size was adjusted during FEM construction to better represent geometric curvatures based on the size of the model. Due to the difficulties involved in meshing a structure with multiple complex interfaces, a formal mesh convergence study was not performed. However, as part of another study, the airfoil section of the fan blade was remeshed with 105,023 three-dimensional continuum shell (SC8R) elements and a modal analysis was performed to determine the natural frequencies of the fan blade. The difference in the modal frequencies for the two models were 5.7% and 9.2% for the first and second modes, respectively, which is considered an acceptable comparison considering that the shell has regions of duplicated mass due to intersecting surfaces that the solid model does not. Therefore, the current shell model is considered to be converged.

In Table 3, the weight and CG locations for an average as-built fan blade and the FEM are presented [16]. For percent error in the CG locations, the differences in the X-, Y-, and Z-dimensions are normalized by the pin width (19.2 in.), the platform height (22.8 in.), and the fan blade length (58.2 in.), respectively. The analytical CG is within 1.02 in. of the as-built CG. The FEM is 10.7 lbf (4.7%) lighter than the as-built fan blade. The lower weight in the FEM is because numerous smaller components in the fan blade (the pin sleeve, bolts, small tuning weights, resin pockets, etc.) were not modeled due to a lack of documented information about these components.

Table 3. Weight and center of gravity for as-built fan blade and analytical model.

Case	Pin Direction, X (in.)	Depth Direction, Y (in.)	Centrifugal Station, Z (in.)	Weight (lbf)
As-built	-0.105	0.054	15.1	229.6
FEM	-0.214	-0.140	16.1	218.9
Difference, %	-0.57%	-0.85%	1.72%	4.7%

Load conditions from Fort Eustis tests 1, 2, 3, and 6 were applied to the load introduction structures as shown by the yellow arrows in Figure 10a. Implicit nonlinear static analyses were performed for these test cases and strains were extracted from each strain gage (SG). Six SGs (1 to 6) were located at the pin-wrap locations and are shown with red crosses in Figure 11. Four more SGs (19, 20, 47, and 48) were located on the airfoil at a Z-location of 21.5-in., as shown in Figure 11. It was unclear from the drawing if the location of SGs 19 and 20 were defined relative to the X-direction or along an axis parallel airfoil, which had a twist angle of 26.9° at this location. Data for the other 21 SGs from these tests were available but are not reported in this document because their locations in Figure 11 are not specified with any measurements.

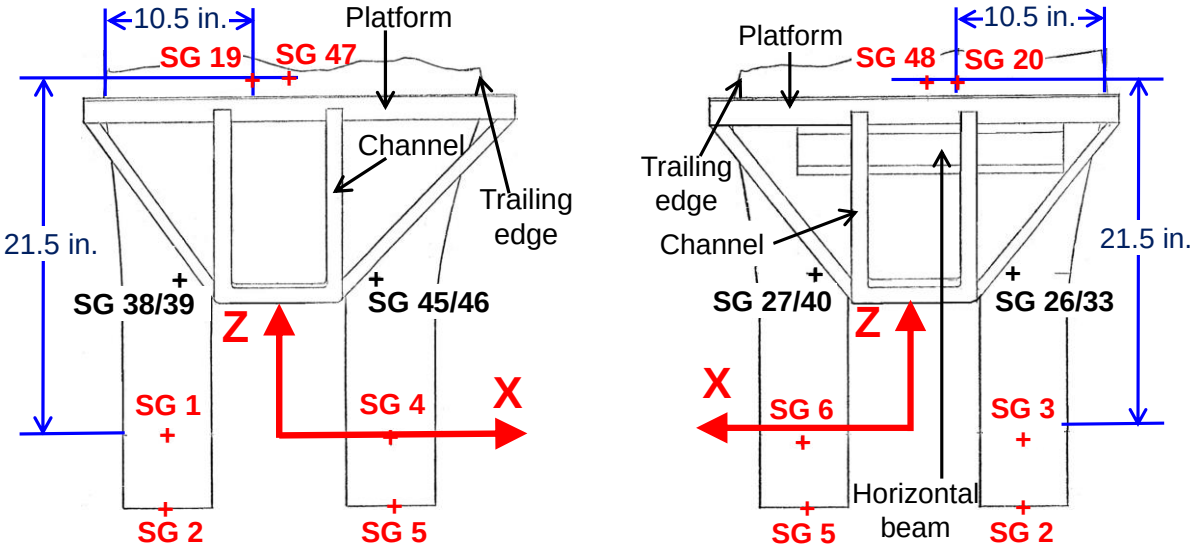

a) Lower surface **b) Upper surface**

Figure 11. SG locations for static tests (SGs shown with red crosses).

VI. Procedure to Determine Unknowns in Tests

The structural model differed from the fan blade that was tested due to both modeling simplifications and unknowns about the details in the model and test fixtures. In the previous study [6], sensitivity of the strain response to the load application position was investigated using a heuristic approach. In this section, a response surface-based optimization approach is described as an expansion of the previous study. Also, additional parameters describing the load fixture (gap between the pin-wraps and the pin, gap between the pin-wraps and the side fixtures, friction, etc.) were used as variables in the optimization study to best match the strain results of the model to the test conditions. Results of the optimization studies are presented in sections VII and VIII.

A. Response Surface-Based Optimization and Analysis of Variance

A design tool called LS-OPT [21] was selected to aid in evaluation of the sensitivity of the strain gages to test fixture unknowns because of its capabilities for graphically displaying the design space, for importing tables of previously generated data into the optimization process, and for evaluating sensitivities of responses to input variables. Additionally, the LS-OPT software can be set up to run any command-line driven code, such as a Python script or a FEA code. The LS-OPT software is used to perform optimization on a response surface (an interpolation technique) representing the selected objective as a function of the design variables. Multiple criteria are available for selection of sets of design variables in the response surface trials, including Latin Hypercube Sampling (LHS) and full factorial methods [22]. LHS is a statistical method for generating a set of nearly random sample points for a multidimensional set of parameters. LS-OPT then automatically partitions runs for the selected analysis code at each trial (set of design variables). Computed results from all trials are used to construct response surfaces, and optimization is performed using those response surfaces. For the studies in this report, the Kriging method was used [23] to generate response surfaces. Kriging is a method for approximating deterministic computer experimental values using a Gaussian correlation function. Adaptive simulated annealing (ASA) [24] was used for the optimization process. ASA is a probabilistic method for approximating the global optimum of a function that does not tend to become stuck in local optima like most gradient descent algorithms. For each optimization study, a maximum number of iterations was defined as the convergence criterion, with more iterations allowed in the final study for each load case.

The design study was performed within LS-OPT as follows (shown in Figure 12):

1. Use LHS within LS-OPT, to select *N* combinations of design variables
2. Create a FEM for each set of design variables
3. Perform ABAQUS analyses of each model
4. Extract the strain responses from every model at every selected SG location
5. Construct a Kriging response surface to approximate the strain response at each SG.
6. Perform an optimization using ASA to minimize the error in the computed strains
7. Reduce the size of the design space for the next iteration
8. Return to step 1 if the convergence criterion is not met, otherwise report the optimum design.

For this study, a Microsoft disk operating system (DOS)-based batch file was used to execute an ABAQUS analysis, and two Python scripts were used to extract strain results from the ABAQUS output databases. One approach to visualize the multidimensional Kriging response surface is to extract two-dimensional (2D) cross sections of the design space in which two design variables are changed while the others are set to their optimum value. These 2D cross sections of the Kriging response surface for a single SG or a combined function representing the response of all SGs can be represented graphically.

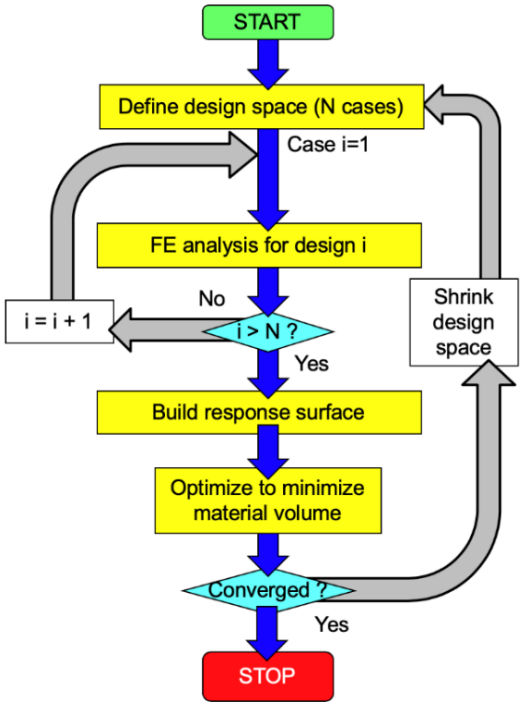

Figure 12. Optimization flowchart.

B. Selection of Unknown Parameters as Design Variables

The FEM of the NTF fan blade was not an exact representation of the fan blade due to unknowns about the geometry and simplifications in the modeling effort. For example, the syntactic foam regions in the LE and TE of the airfoil were not modeled due to unknowns in their material properties. Also, in Figure 11, the assumed locations of the SGs were provided for the centrifugal (Z-station) direction but not for the pin (X) axis direction; so, the assumed locations of some of the SGs may differ slightly from the as-tested specimen. Additionally, several small structures, including the horizontal beam shown in Figure 11b were not modeled due to limited geometric dimensions. These many dimensional and material unknowns made test-analysis correlation difficult.

The test fixtures were not modeled explicitly; because, neither engineering drawings nor material properties were available. Also, important details such as the exact application points for the centrifugal loads as well as the orientation of the fan blade in the static test fixture were unknown and are approximated based on Figures 8 and 9. In Ref [15], slippage at the fixtures and flexibility of the fixtures was noted, which could account for the nonlinear behavior in the test data that is not captured by the analysis. As noted previously, characterization of the fixture response and boundary response is needed for more accurate modeling, and therefore, improve test-analysis correlation [9,10]. Unfortunately, such information is not usually available for legacy tests, so the optimization approach was applied in order to obtain the necessary level of test-analysis correlation for model validation.

Several unknown parameters were selected for use as design variables in optimization studies to improve the test-analysis correlation. The X and Y coordinates for the application point of the centrifugal load were used (those variables had also been used in the previous study [6]). The unknown rotated angle of the fan blade in the test fixture affected the strain response to aerodynamic loading. Gaps between the test fixtures and the test specimen (the NTF fan blade) were also considered to be likely sources of error in the strains. These possible gap locations included between the pin-wraps and the pin, between the bottom of the platform section and the hub, and between the pin-wraps and the sides of the hub. Friction at these gap locations was another unknown.

Therefore, for the centrifugal loading case, three variables were considered important: gap at the pin, and the centrifugal load X and Y coordinates. Because the centrifugal loading was tensile, pin friction and gaps in the hub should not have significantly affected the strain response in centrifugal loading. For the aerodynamic load case, six variables were considered important: gap at the pin, friction at the pin, fan blade rotation angle, and gaps at the three hub surfaces (top of hub and two sides, as shown in Figure 10a). Note that only the gap between the pin and pin-wraps was expected to have a major influence on the strain response to both centrifugal and aerodynamic loading.

VII. Test-Analysis Correlation for Load Case 1

In the previous study [6], strains were only evaluated at four SGs, two in the pin-wrap section (SGs 2 and 5), and two at the fan blade root (SGs 19 and 20), as shown in Figure 11. In the previous study, sensitivity of the strains was evaluated by changing the centrifugal load application point at three locations. To expand upon this earlier study, the LS-OPT software [21] was used to construct a response surface for each strain response, and then the optimization tools within LS-OPT were used to minimize the difference in the strains for the numerical model and the test data. In this section, test-analysis correlation was performed for load case 1, in which only a centrifugal load was applied. Test-analysis correlation for other load cases is discussed in later sections.

A. Sensitivity of Strain Results to Centrifugal Load Application Position

As a first step, sensitivity of the strain response in the numerical model to the centrifugal load application position (using X- and Y- locations as shown in Figure 13) was investigated. In Figures 14a to 14d, Kriging response surfaces for SGs 2, 5, 19, and 20, respectively, are presented. The response surfaces were created from a set of nine data points, shown as green squares in the figures. Upper and lower bounds on the X and Y coordinates were set at +1.0 in. and -1.0 in. based on initial evaluations of the variations in the strain response. In the figures, the error in the strains (numerical model strains minus strains from test data) are represented by colored bands that vary with the load application position (X and Y coordinates). In Figures 14a and 14b, the contour corresponding to a strain error of zero is shown as a dashed red line. The red lines in Figures 14a and 14b are nearly parallel to each other but are about 0.2 in. apart. Contours with zero strain error are not visible in Figures 14c and 14d, because the error in the strains at the pin location is very high (between 300 and 1000 microstrain). To isolate the effects of the variables on each set of responses, a rotated coordinate system was developed based on the zero-error contours for SGs 19 and 20. This rotated coordinate system is identified as X' and Y' axes in Figure 13. An angle of 25.6° was determined from the contours in Figures 14a and 14b with a Y-intercept value of -0.24. The y-intercept value and corresponding X value (0.50) were selected because they are between the dashed lines in Figures 14a and 14b. The transformation between the rotated local coordinate system (X' and Y') and the global coordinates was computed using Equations 1 and 2.

$$X = X' \cos(25.6) - Y' \sin(25.6) + 0.50 \quad (1)$$

$$Y = X' \sin(25.6) - Y' \cos(25.6) - 0.24 \quad (2)$$

Kriging response surfaces for the error in the strains in the rotated local coordinate system (X' and Y') are presented in Figures 15a to 15d. In Figure 15a and 15b, the strain contours are parallel to the X' axis, indicating that the strains in the airfoil section (SGs 19 and 20) are primarily influenced by the Y' location and are independent of the X' location. Also, the error in computed strains in SGs 19 and 20 approach a value of zero at a Y' value of 0.0. In Figure 15c and 15d, the strain contours are parallel to the Y' axis, indicating that the strains in the pin-wrap section (SGs 2 and 5) are primarily influenced by the X' location and are independent of the Y' location. Unfortunately, a zero error in the computed strains in SGs 2 and 5 did not occur at the same X' value, and in fact, reduction of the error in each SG is in the opposite direction. To determine the best combination of the X' and Y' location variables to match the test data, an optimization was performed using these response surfaces.

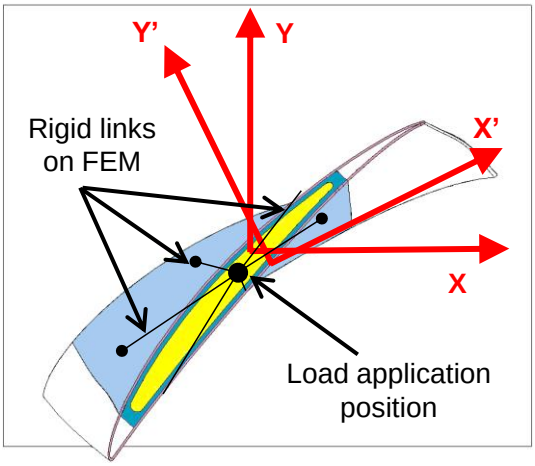

Figure 13. Variation of load application position.

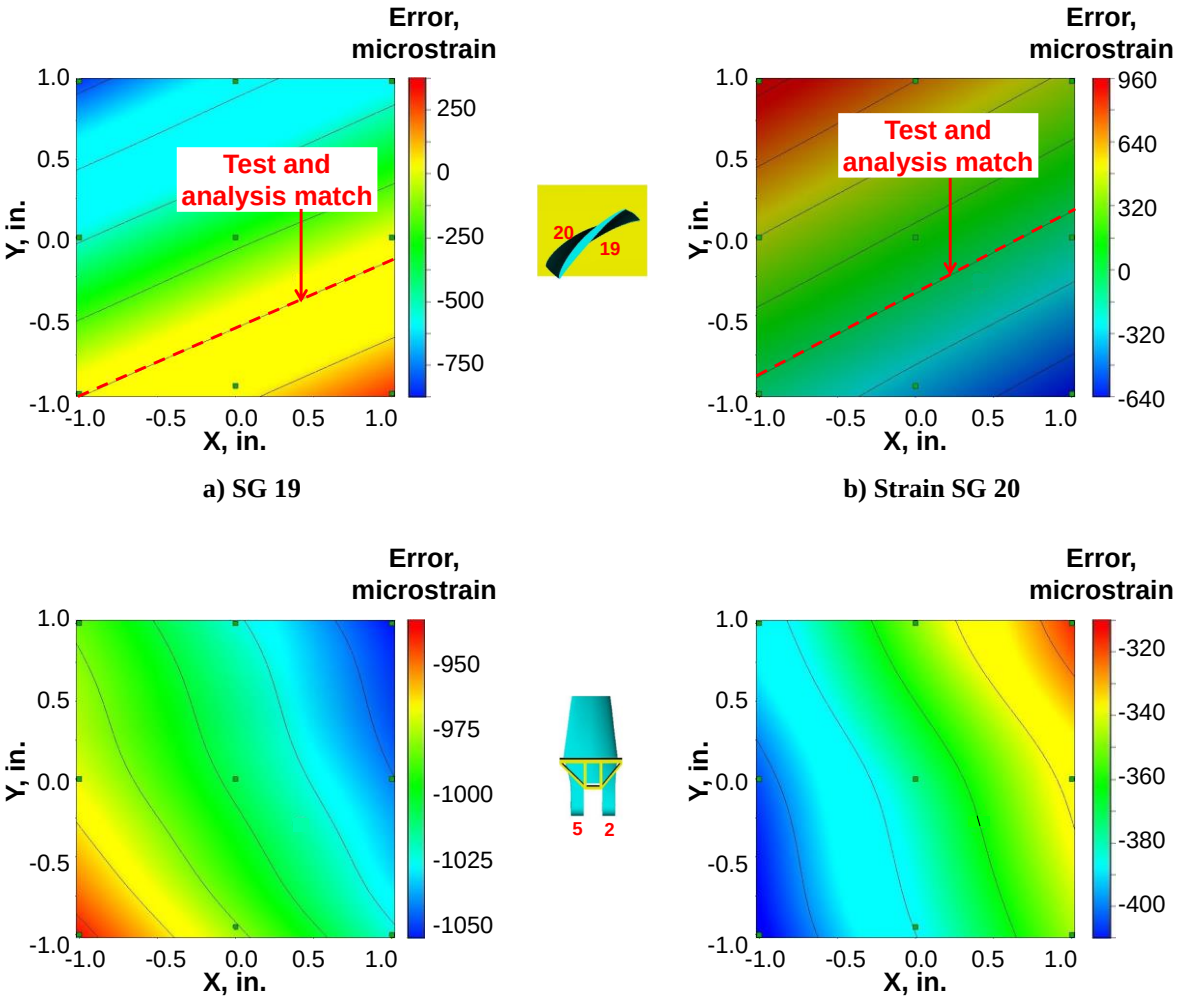

a) SG 19

b) Strain SG 20

c) SG 2

d) SG 5.

Figure 14. Sensitivity of strains to location of applied load (X- and Y-coordinates) for load case 1.

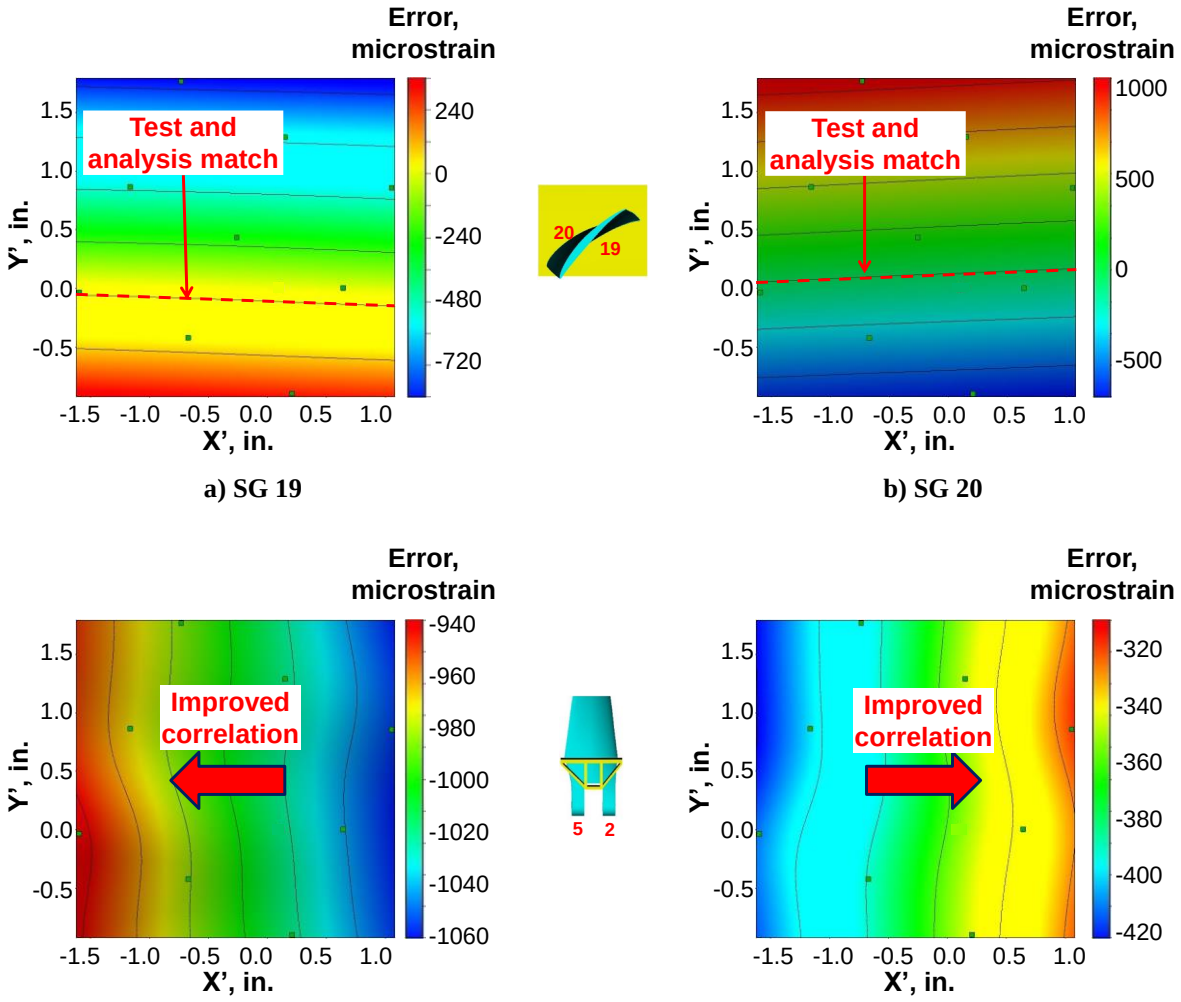

Figure 15. Sensitivity of strains to location of applied load (X'- and Y'-coordinates) for load case 1.

Optimization was performed to minimize the computed error in the SGs. The objective function to minimize was selected as an average root means square (ARMS) error at maximum load (57 kips), computed using Equation 3. In Equation 3, the strain (ε) at maximum load is evaluated for a selected number of SGs, N. Two optimization studies were conducted. In the first optimization study, the strain responses from only four SGs (N=4) were used. For the second study, nine of the ten SGs identified in Figure 11 were used (SGs 1, 3 to 6, 19, 20, 47, and 48). Based on the response in Figure 15c and the responses of the other SGs, reducing the error in SG 2 was observed to increase the error in the other SGs, so it was excluded from the ARMS equation in the second study. Constraints on the optimization are upper and lower limits on the X' (-1.5 in. to 1.0 in.) and Y' (-1.0 in. to 2.0 in.) values. Based on the initial response surfaces, these constraint limits were judged to be likely to bound the optimum point. Only one iteration was used for convergence. ARMS error contours for the two studies are shown in Figures 16a and 16b. In both cases the optimum point occurred at a Y' value of 0.0. But for the first study, the optimum value of X' was less than the selected limit on X', and hence outside the design space. In the second study, the optimum value for X' was at 0.0. Because the optimum point was well within the design space and because it used more strain responses, for all further studies with load case 1, the ARMS equation with nine SGs was used. The optimum load application location (X'=0.0 in. and Y' = 0.0 in.) will be referred to herein as optimum #1.1 as identified in Figure 16b.

$$ARMS = \frac{\sqrt{\sum_{i=1}^{N}\left(\varepsilon^{i}_{Computed} - \varepsilon^{i}_{Test}\right)^{2}}}{N} \qquad (3)$$

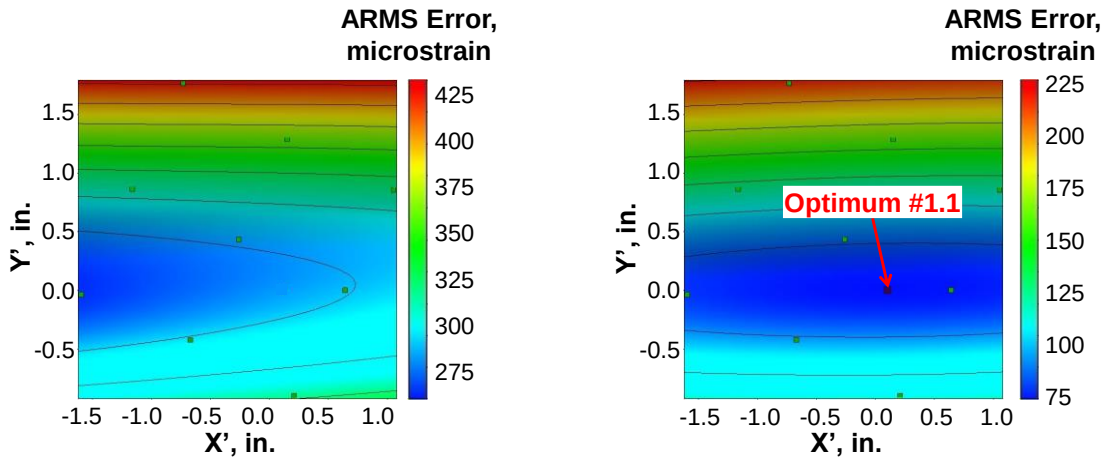

a) ARMS error computed for 4 SGs **b) ARMS error computed for 9 SGs**

Figure 16. Sensitivity of ARMS error to location of applied load (X'- and Y'-coordinates) for load case 1.

Strain data from the tests [15] and from the FEA at optimum #1.1 for load case 1 are reported in Figures 17 to 20. Strains during the unloading phase of the tests were available but are not plotted because they tended to follow the loading curves and for clarity of the figures. From the test data, strains in the airfoil section (Figures 17 and 18) exhibited linear behavior. Test and analysis results agreed within 80 microstrain in the SGs on the airfoil section, SGs 19, 20, 47, and 48. As shown in Figures 19 and 20, the FEA results were significantly lower than the test data at the pin-wraps (74% and 49% lower for SGs 2 and 5, respectively), but the shapes of the analytical strain-load curves were similar at higher loads. Correlation was similarly poor for the pin-wrap section SGs in Figure 20, and the percentage error is higher (up to -717%) than in Figure 19 because the SG values are very low (less than 200 microstrain) at maximum load. The slopes of the strain curves from both analysis and test in the pin-wrap section SGs matched well, but the significant nonlinearity in the initial loading was not predicted by the analysis. Optimization for just the X' and Y' locations did not improve the correlation significantly from the previous study [6], and the correlation in the pin-wrap section SGs was poor; therefore, it was necessary to look at other sources of unknowns in the computed strain results. The notes from the test in 1981 [15] mentioned "slop" in the test setup. This issue with the test fixtures is discussed in the next section.

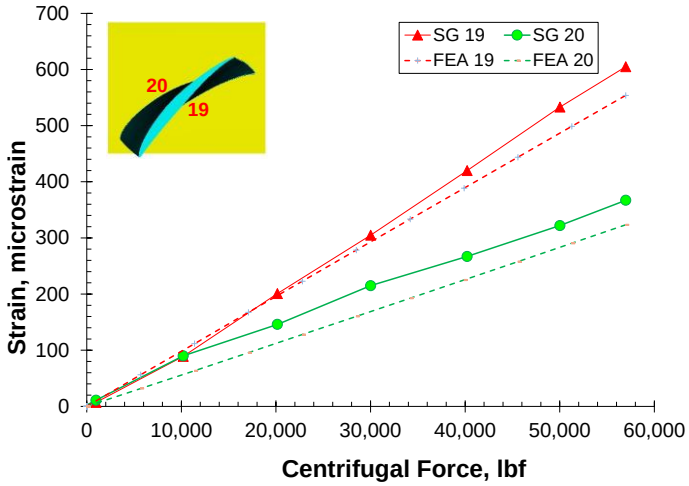

Figure 17. Strain vs. load test-analysis correlation at optimum #1.1 for load case 1 (SG 19 and 20).

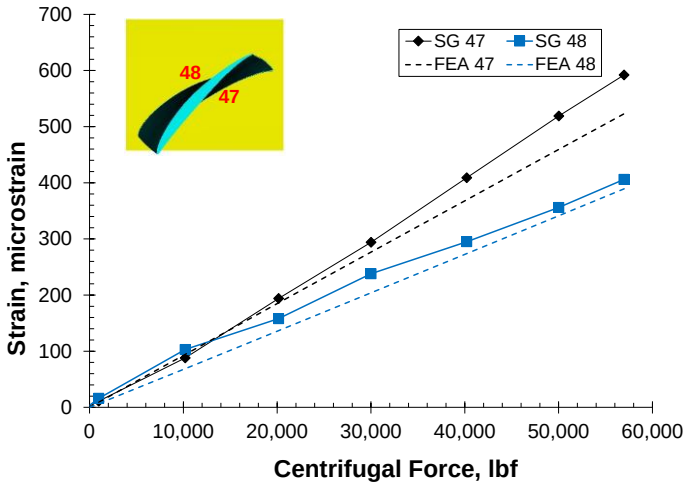

Figure 18. Strain vs. load test-analysis correlation at optimum #1.1 for load case 1 (SG 47 and 48).

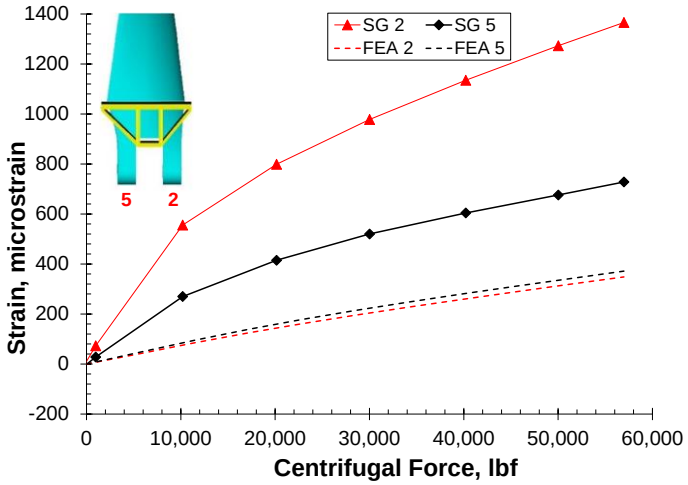

Figure 19. Strain vs. load test-analysis correlation at optimum #1.1 for load case 1 (SG 2 and 5).

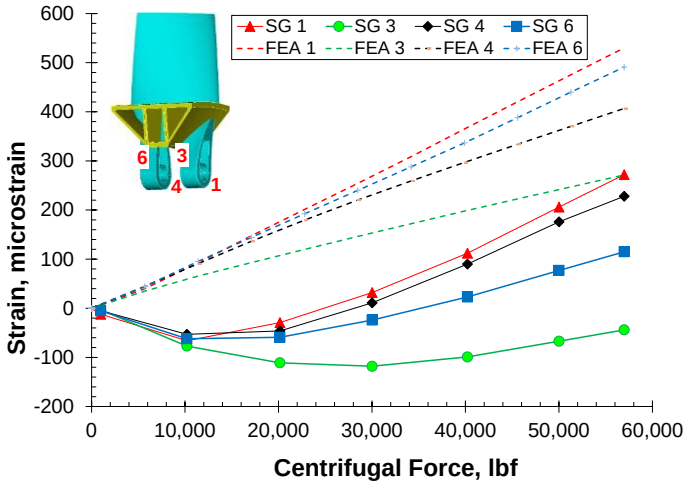

Figure 20. Strain vs. load test-analysis correlation at optimum #1.1 for load case 1 (SG 1,3,4, and 6).

B. Sensitivity of Strain Results to Centrifugal Load Application Position and Gap at Pin

Notes from the test in 1981 [15] refer to slippage of the specimen during testing, due to some unexpected flexibility in the test setup. Based on the test documentation and experience with pinned test fixtures [9], one possible cause of slippage in the test specimen under centrifugal loading was a gap between the pin and the pin-wrap section of the fan blade. In the FEM the pin and sleeve were modeled together as a rigid analytical surface as illustrated in Figure 21. In the FEM, this gap was modeled as a reduction in the diameter of the analytical rigid cylinder representing the pin and sleeve, and the gap is referred to as the "gap at pin" in the rest of this report. In this section, sensitivity of the computed strains to the Y' location and the pin gap are evaluated, and the value of the X' variable is set to 0.0, the value of optimum #1.1.

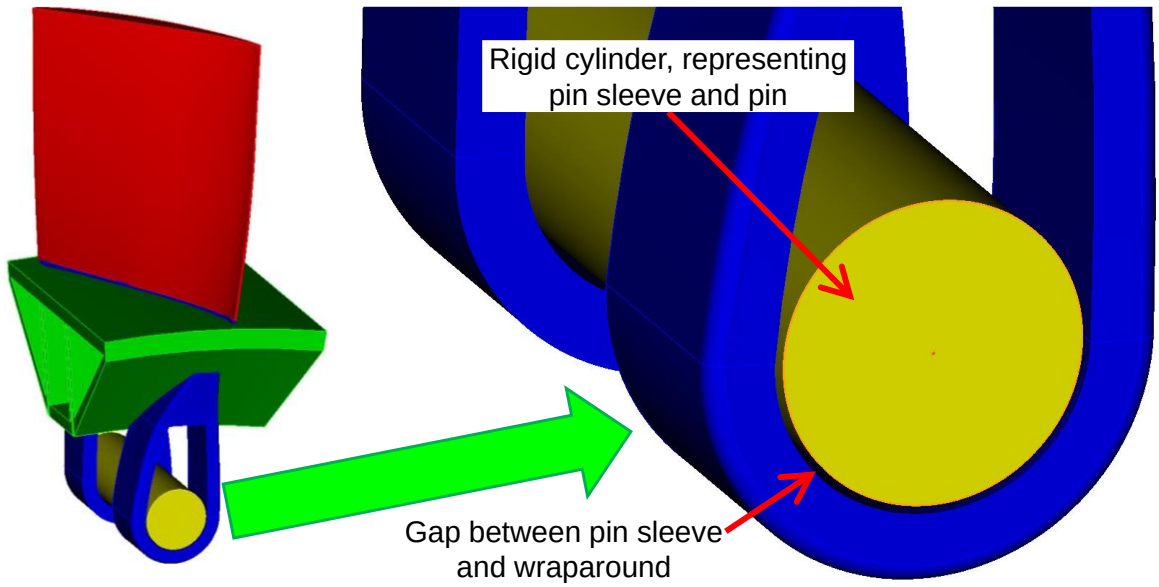

Figure 21. "Gap at pin" between pin sleeve and pin-wrap section of fan blade.

Kriging response surfaces for the error in the strains in the design space for the pin gap and the Y' location are presented in Figures 22a to 22d. The Kriging response surfaces were constructed from the nine initial trial points shown as green squares in Figure 22a to 22d. In Figure 22a and 22b, the strain contours are parallel to the pin gap axis, indicating that the strains in airfoil section (SGs 19 and 20) are primarily influenced by the Y' location and are independent of the pin gap. In Figure 22c and 22d, the strain contours are parallel to the Y' axis, indicating that the strains in the pin-wrap section (SGs 2 and 5) are primarily influenced by the pin gap and are independent of the Y' location. Also, the error in the computed strains for SG 5 approach a value of zero at a pin gap value of 0.012 in. Another optimization study was performed to determine the best combination of the pin gap and Y' variables.

Optimization was performed to minimize the computed error in the SGs using the 9 SG ARMS objective function. ARMS error contours for this second study are shown in Figure 23. Constraints on the optimization are upper and lower limits on the Y' (-0.5 in. to 0.5 in.) and gap at pin (0.00 in. to 0.02 in.) values. During this optimization study, only one iteration was performed for convergence. The optimum point (labeled optimum #1.2 in the figure) occurred at a Y' value of 0.0052 in. with a pin gap of 0.01014 in. The ARMS error at the maximum 57 kip load dropped from 77 microstrain at optimum 1.1 to 23 microstrain at optimum 1.2. A final optimization study is presented in the next section in which all three variables were considered in the design process. Also, because the strain response in the pin-wrap section is nonlinear, the ARMS equation in the next section includes SG values at a lower load (20 kips).

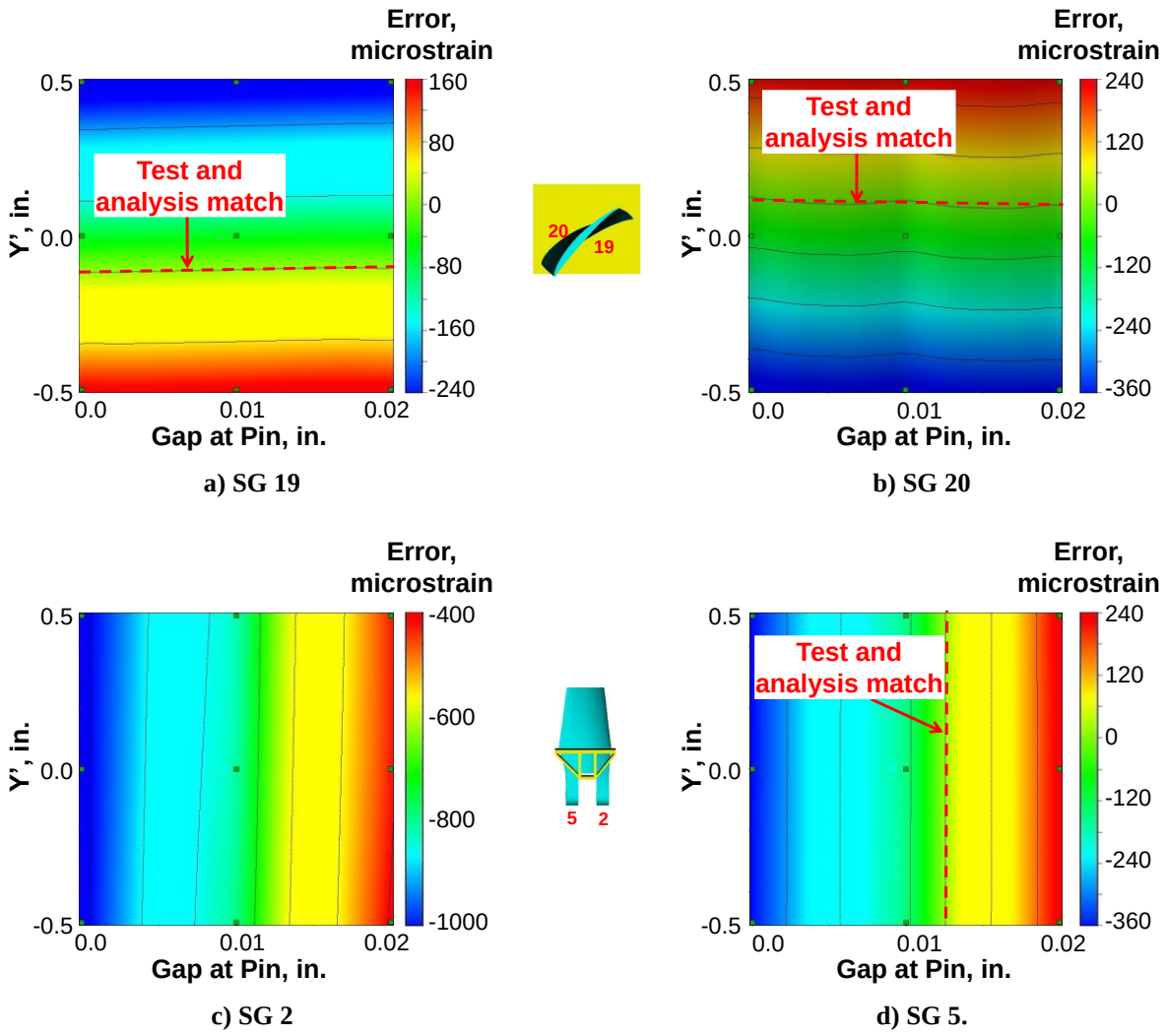

a) SG 19

b) SG 20

c) SG 2

d) SG 5.

Figure 22. Sensitivity of strains to gap at pin and location of applied load (Y' coordinate) for load case 1.

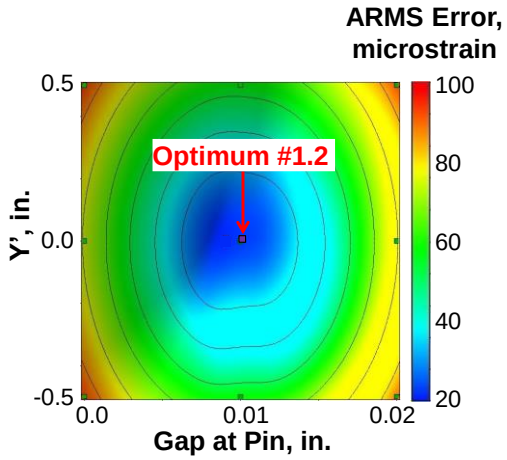

Figure 23. Sensitivity of ARMS error to gap at pin and location of applied load (Y' coordinate) for load case 1.

Strain data from the tests [15] and from the FEA at optimum #1.2 for load case 1 are reported in Figures 24 to 27. Strains during the unloading phase of the tests were available but are not plotted for clarity of the figures. Test and analysis results agreed within 66 microstrain in the SGs on the airfoil section (Figures 24 and 25), which is only a slight improvement (from 21% to 18% maximum error) over optimum #1.1. Due to a small uncertainty in the SG location, selection of an adjacent element for post-processing could improve the results in the airfoil section (particularly SG 20), but the expected improvement was deemed to be very small and therefore was not computed. The FEA results in the pin-wrap region improved significantly from optimum #1.1, with the error in SGs 1 and 3 to 6 varying from 0 to 109 microstrain, as shown in Figures 26 and 27. Correlation in SG 2 improved from an error of 1018 microstrain to 757 microstrain (74% to 55%), but this error is still large. Considering that the response in SG 2 is inconsistent with the responses in the other LE pin-wrap section SGs (SG 1 and SG 3, which are located close to SG 2), results for this SG are ignored in the evaluation of the test-analysis correlation for load case 1. In the next section, all three variables were included in the optimization as a final attempt to improve the correlation. Also, in the next section the error and percent error at maximum load for each SG are presented in tabular format for three optima.

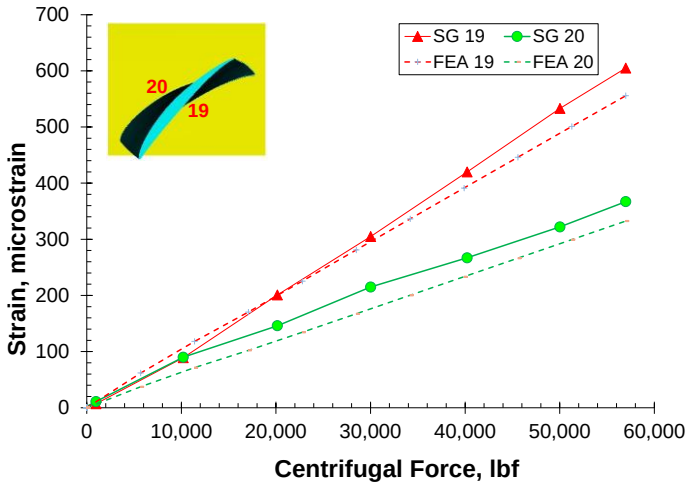

Figure 24. Strain vs. load test-analysis correlation at optimum #1.2 for load case 1 (SG 19 and 20).

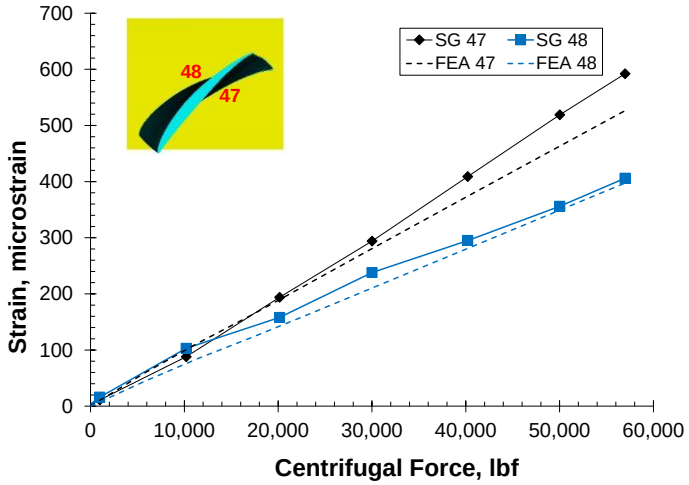

Figure 25. Strain vs. load test-analysis correlation at optimum #1.2 for load case 1 (SG 47 and 48).

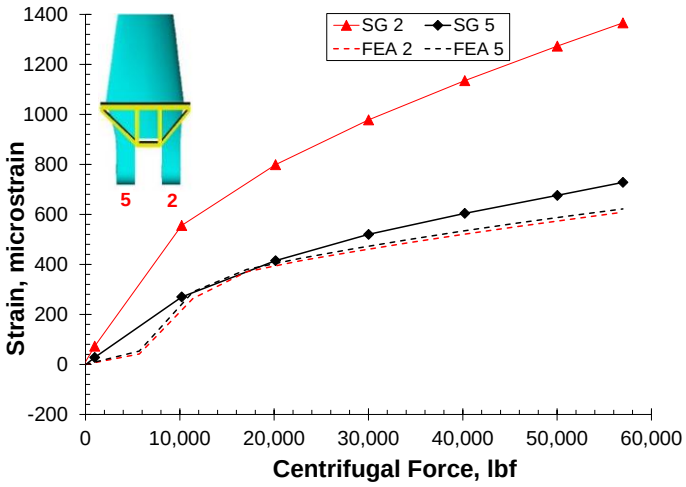

Figure 26. Strain vs. load test-analysis correlation at optimum #1.2 for load case 1 (SG 2 and 5).

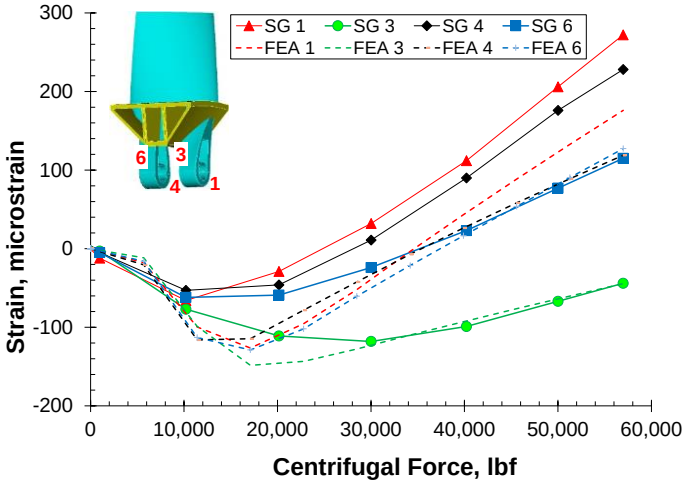

Figure 27. Strain vs. load test-analysis correlation at optimum #1.2 for load case 1 (SG 1, 3, 4, and 6).

C. Sensitivity of Strain Results to Centrifugal Load Application Position and Gap at Hub

For the third optimization study, three variables (pin gap and the X' and Y' location variables) were used to minimize the computed error in the SGs. The objective function to minimize was selected as an ARMS error for nine SGs at two load levels (20 kips and 57 kips). ARMS error contours for this three-variable study are shown in Figures 28a and 28b. Constraints on the optimization are upper and lower limits on the X' location (-0.8 in. to 0.0 in.), Y' location (-0.5 in. to 0.5 in.), and gap at pin (0.008 in. to 0.013 in.) values. During this optimization study, five iterations were performed in which the design space was reduced (centered on the optimum from the previous iteration) to improve the quality of the response surface, as illustrated by the additional trial points shown in Figures 28a and 28b. The three-dimensional design space is difficult to represent graphically, so instead two-dimensional cross sections through the design space are shown. In Figure 28a, the value of X' was held constant (at a value of -0.2760 in.) while the pin gap and Y' were varied. In Figure 28b, the value of the pin gap was held constant (at a value of 0.00971 in.) while X' and Y' were varied. The values for the optimum point (labeled optimum #1.3 in Figures 28a and 28b) are presented in Table 4. As shown in Table 4, the ARMS error using two load levels improved slightly from 13.0 microstrain to 12.7 microstrain. A comprehensive list of the errors and percent error in all SGs at the maximum (57 kip) load level is presented in Tables 5 and 6, respectively, for all three optima. In Table 5, error values less than 100 microstrain indicate good agreement and are shown in green, values between 100 and 200 microstrain are considered moderate agreement and are shown in yellow, and values greater than 200 microstrain are considered poor agreement and are shown in red.

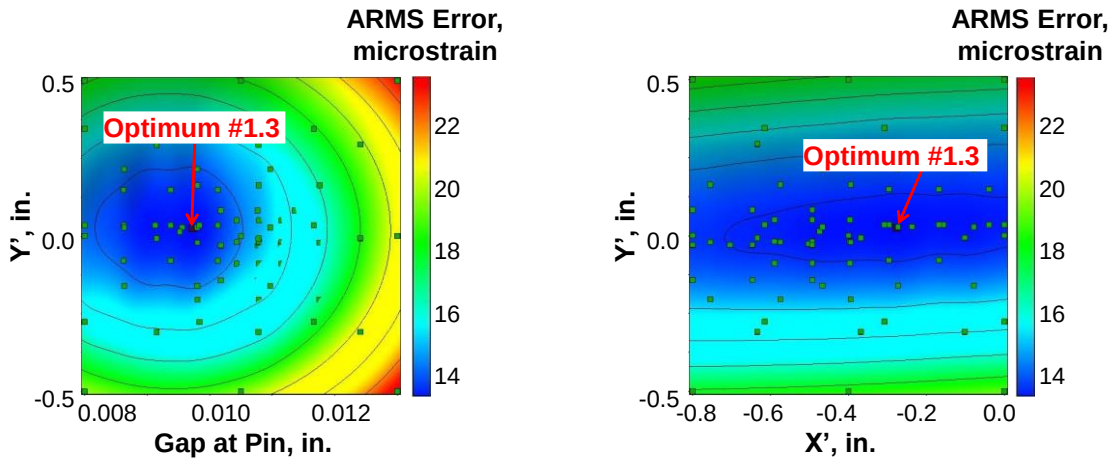

a) ARMS variation with pin gap and Y' location (X' location = -0.276 in.)

b) ARMS variation with X' and Y' location (gap at pin = 0.00971 in.)

Figure 28. Sensitivity of ARMS error in strains to pin gap and X' and Y' location variables for load case 1.

Table 4. Design variable and ARMS error values for optimum points 1.1 to 1.3 for load case 1.

Optimum	X', in.	Y', in.	Pin Gap, in.	ARMS at 20-kip Load, microstrain	ARMS at 57-kip Load, microstrain	ARMS at 20- and 57-kip Load, microstrain
1.1 (X', Y')	0.0000	0.0000	0.00000	55.73	76.67	47.39
1.2 (Gap at Pin, Y')	0.0000	0.0052	0.01014	13.28	22.38	13.01
1.3 (Gap at Pin, X', Y')	-0.2760	0.0102	0.00971	11.38	22.65	12.67

Table 5. Error in computed SG values for optimum points 1.1 to 1.3 for load case 1.

Optimum	Error in Computed Strains at 57-kip Load, microstrain									
	Pin-Wrap Section						Airfoil Section			
	SG 1	SG 2	SG 3	SG 4	SG 5	SG 6	SG 19	SG 20	SG 47	SG 48
1.1 (X', Y')	258	-1018	316	179	-357	376	-51	-44	-69	-17
1.2 (Gap at Pin, Y')	-96	-757	0	-109	-106	12	-49	-34	-66	-9
1.3 (Gap at Pin, X', Y')	-74	-761	15	-106	-129	-2	-47	-25	-70	-3

Table 6. Percent error in computed SG values for optimum points 1.1 to 1.3 for load case 1.

Optimum	Percent Error in Computed Strains at 57-kip Load									
	Pin-Wrap Section						Airfoil Section			
	SG 1	SG 2	SG 3	SG 4	SG 5	SG 6	SG 19	SG 20	SG 47	SG 48
1.1 (X', Y')	95%	-74%	-717%	78%	-49%	327%	-8%	-12%	-12%	-4%
1.2 (Gap at Pin, Y')	-35%	-55%	1%	-48%	-15%	11%	-8%	-9%	-11%	-2%
1.3 (Gap at Pin, X', Y')	-27%	-56%	-35%	-47%	-18%	-2%	-8%	-7%	-12%	-1%

As shown in Table 5, SGs in the airfoil section were in good agreement with FEA results, and SGs in pin-wrap section (except SG 2) were in good to moderate agreement with FEA results. In Table 6, the percentage error at maximum load is less than 12% for the SGs in the airfoil section, but the percent error is up to 56% for the SGs in the pin-wrap section. Because of the large variation in magnitude of the strain response among different SGs and the variation in the strain response at different load levels, to evaluate the errors in the FEA results, comparison of the SG responses at multiple load points is preferred.

Strain data from the tests [15] and from the FEA at optimum #1.3 for load case 1 are reported in Figures 29 to 32. The FEA results improved only slightly for optimum #1.3 compared to optimum #1.2. Because of the improvement compared to the original correlation study and lack of improvement in the last correlation study, investigation of additional test fixture parameters was deemed to be unlikely to improve the results. The pin gap and centrifugal load location from optimum #1.3 were used as fixed parameters in the test-analysis correlation studies in the remaining sections of this report.

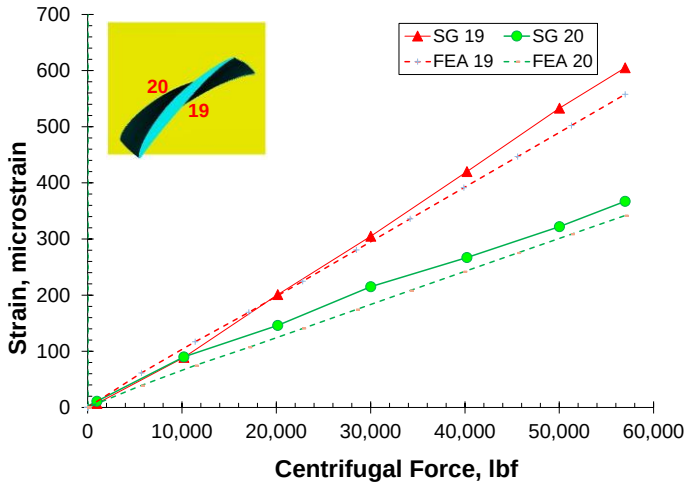

Figure 29. Strain vs. load test-analysis correlation at optimum #1.3 for load case 1 (SG 19 and 20).

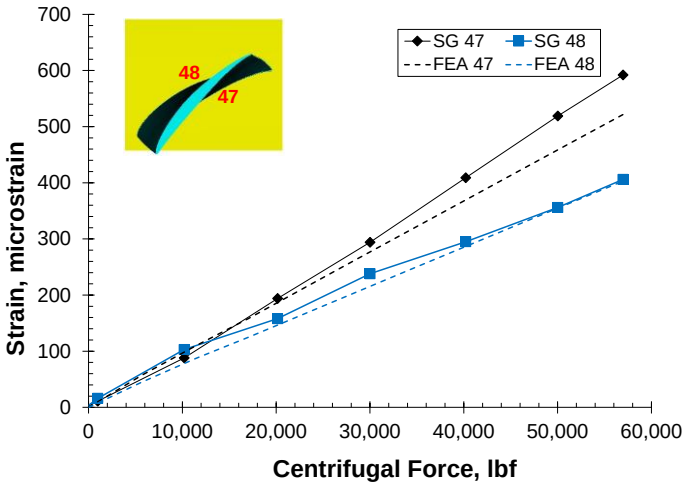

Figure 30. Strain vs. load test-analysis correlation at optimum #1.3 for load case 1 (SG 47 and 48).

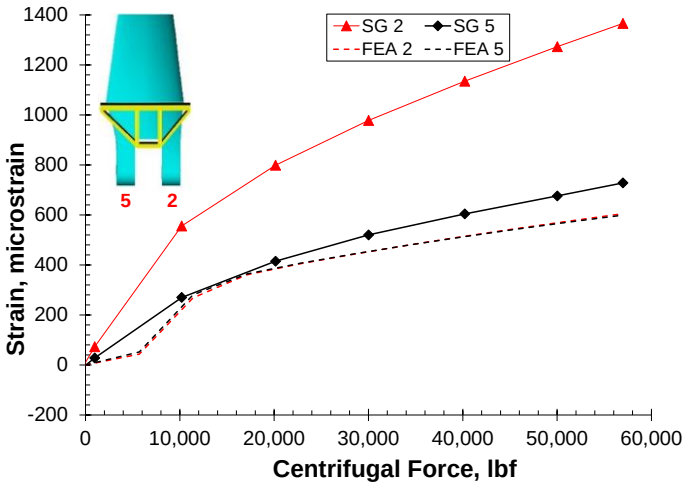

Figure 31. Strain vs. load test-analysis correlation at optimum #1.3 for load case 1 (SG 2 and 5).

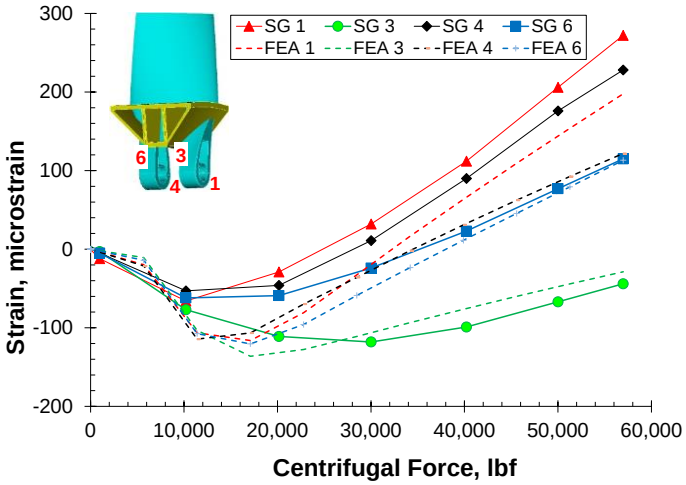

Figure 32. Strain vs. load test-analysis correlation at optimum #1.3 for load case 1 (SG 1, 3, 4, and 6).

VIII. Test-Analysis Correlation for Load Case 2

An optimization study was conducted using the LS-OPT software to minimize the difference in the strains for the numerical model and the test data due to a centrifugal loading in the previous section. In this section, test-analysis correlation was performed for load case 2, in which an approximated aerodynamic loading was applied as shown in Figure 8. For load case 2, a new set of variables was used to represent unknowns in the test fixtures, while the gap at the pin and centrifugal load location variables were held constant at the values of optimum #1.3 from the previous study.

A. Strain Results Based on Optimum #1.3

As an initial check of the strain response, strain data from the tests [15] and from the FEA at optimum #1.3 for load case 2 are reported in Figures 33 to 36. Strains during the unloading phase of the tests were available but are not plotted because they tended to follow the loading curves and for clarity of the figures. From the test data, strains in the airfoil section exhibited linear behavior (Figures 33 and 34). At maximum load, test and analysis results agreed within 12% in three of the SGs (19, 47, and 48) in the airfoil section and within 28% in SG 20. At the end of this section, the error and percent error at maximum load for each SG are presented in tabular format. The magnitudes of the FEA results were lower than the test data at the pin-wrap region (Figures 35 and 36), but the nonlinear shapes of the curves are similar. In the next sub-section, five test fixture variables affecting the strain response due to aerodynamic loading (pin friction, fan blade rotation angle, and three gaps between the hub and the fan blade) are discussed. For load case 2, the strain results for SG 2 seemed consistent with the responses in the other pin-wrap section SGs; so, all ten SGs were used in the ARMS error function for the optimization study performed in the following sub-sections.

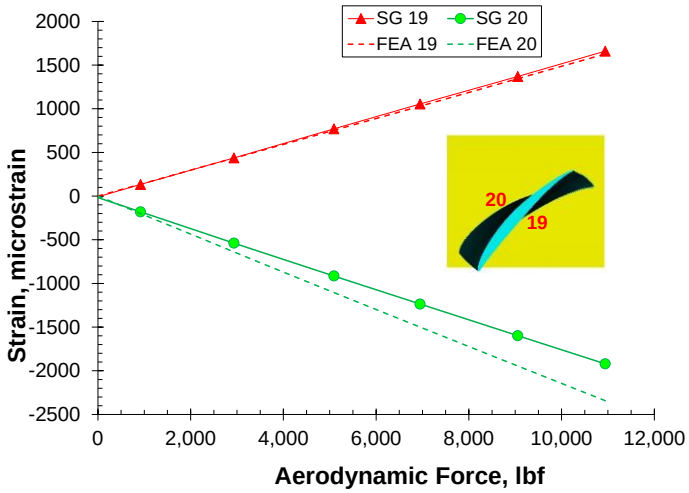

Figure 33. Strain vs. load test-analysis correlation at optimum #1.3 for load case 2 (SG 19 and 20).

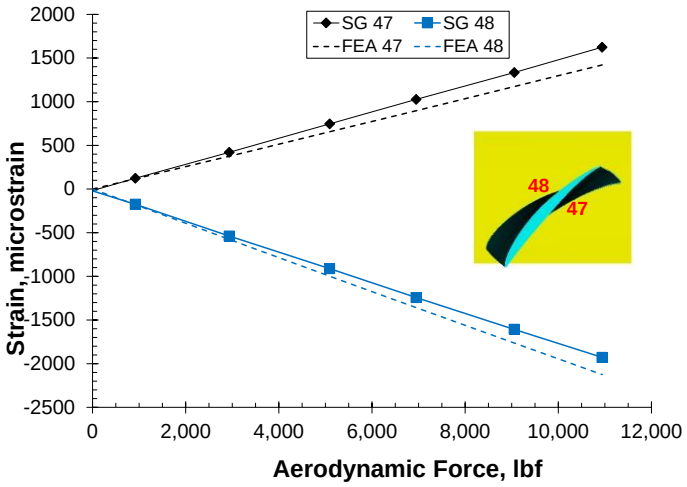

Figure 34. Strain vs. load test-analysis correlation at optimum #1.3 for load case 2 (SG 47 and 48).

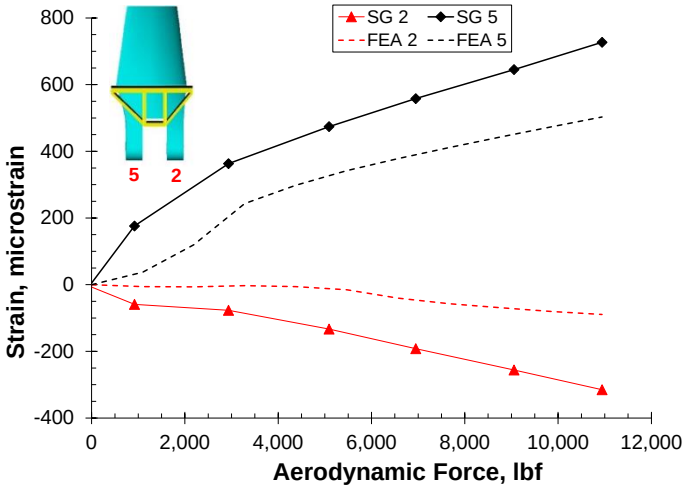

Figure 35. Strain vs. load test-analysis correlation at optimum #1.3 for load case 2 (SG 2 and 5).

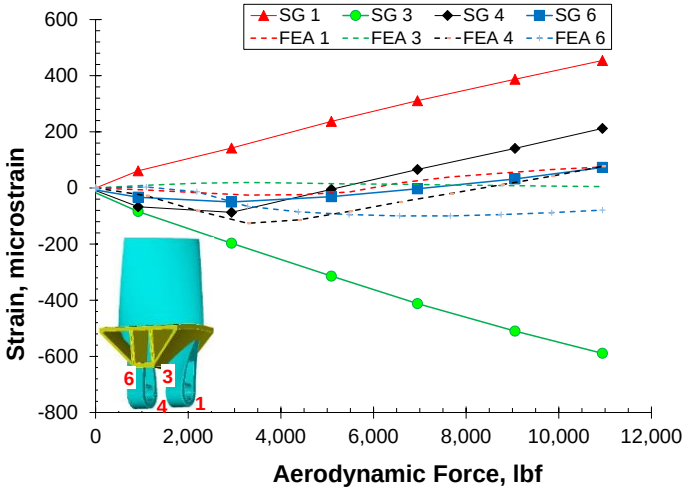

Figure 36. Strain vs. load test-analysis correlation at optimum #1.3 for load case 2 (SG 1, 3, 4, nd 6).

B. Screening of Unknowns in Test Fixtures

Based on the test documentation and experience with test fixtures in other tests [9,10], one possible cause of slippage in the test specimen under aerodynamic loading was likely to have been a gap between the hub and the fan blade. As shown in Figure 10a, the hub is represented with three surfaces, a cylindrical top surface, a flat surface on the LE side of the fan blade, and another flat surface at the TE of the fan blade. Herein, these three gaps between the rigid hub and the fan blade are respectively referred to as the "gap at top of hub," "gap at LE of hub," and "gap at TE of hub." The gap at the top of the hub was modeled as a reduction of the radius of curvature of the surface. Similarly, gaps at the LE and TE of the hub were represented by changes in location of the surfaces in the global X direction. During application of the aerodynamic load, changing the gap dimension changes the angle at which the root and platform sections contact the hub and potentially affect the strain responses. These gaps were not considered for load case 1, because the hub would not have been in contact with the fan blade during a pure centrifugal loading.

Two other unknowns are associated with the test fixtures. As shown in Figure 8, the fan blade was mounted at an angle, and this angle was defined in the FEM as the angle of the applied aerodynamic load from the global Y axis (rotating about the global Z axis). This angle is not specified in the test documentation [15], but based on Figure 8, the angle appears to have been between -40° and -50°. A fifth unknown considered in the test fixtures for load case 2 was friction reacting against rotation of the fan blade around the pin.

In order to eliminate variables that do not affect the strain response, sensitivity analysis of the variables was performed. Sensitivity of the strain response to the gaps at the LE and TE of the hub was evaluated by performing a parameter study, in which one parameter at a time was varied while the other parameters were fixed. The results of this sensitivity study are presented in Figures 37 and 38. In Figure 37, the ARMS error was essentially a step function with a minimum value of zero, and the variation in the ARMS error due to the gap at the LE of the hub was less than 0.4 microstrain. In Figure 38, the response of the ARMS error to the gap at the TE of the hub was larger than the gap at the LE of the hub, and the response approached an asymptotic minimum at values above 0.04 in. Based on this study, the gap at the LE of the hub was set to a fixed value of 0.020 in. for the test-analysis correlation. The gap at the TE of the hub was still used as a variable because the optimum value for the gap seemed to behave more like an asymptotic curve than a step function and might change based on the other variables.

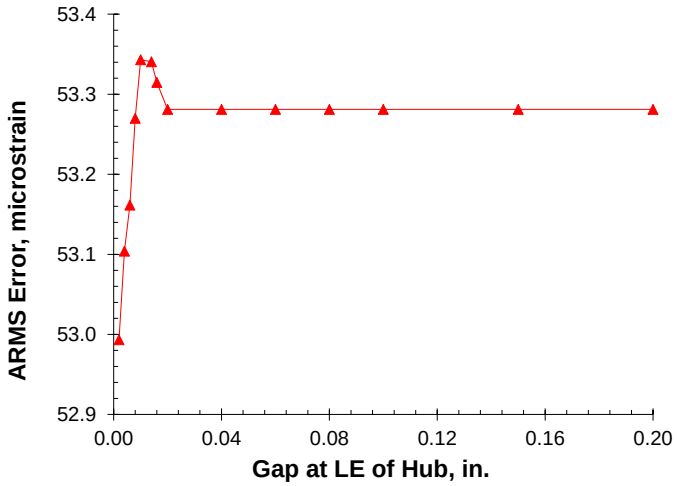

Figure 37. Parameter study of ARMS error for load case 2 to gap at LE of the hub.

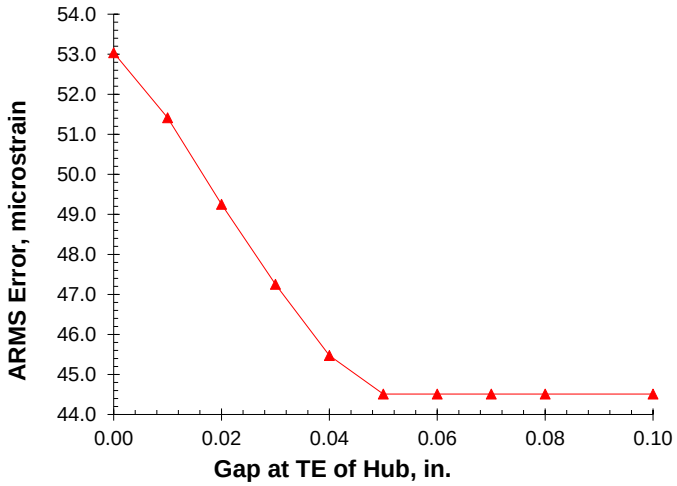

Figure 38. Parameter study of ARMS error for load case 2 to gap at TE of the hub.

While the parameter study above is one standard approach, it is highly dependent on the selection of the nominal values of the parameters. Another standard approach for sensitivity studies is called analysis of variance (ANOVA) [24]. In classical ANOVA studies, data is collected from multiple experiments (function evaluations) while both varying all parameters and varying one parameter at a time. The LS-OPT software includes some ANOVA-based tools including the global sensitivity analysis (GSA) method developed by Sobol [24, 25]. In LS-OPT, GSA was performed using a Monte Carlo simulation with 10,000 points with the function evaluations performed by the response surfaces. The result of the GSA study was a ranking of the influence of each parameter on the response surface function values, as shown in Figure 39 for the five variables in load case 2. In Figure 39, the influence of the LE gap on all responses was very low for all SGs and for the aggregate ARMS error responses, justifying exclusion of this variable from optimization studies. SGs in the pin-wrap section were strongly influenced by friction and the TE gap, and SGs in the airfoil section were strongly influenced by the angle of the applied load. The gap at the hub gap had a large effect on the ARMS error responses because of the large error in the response of SG 5.

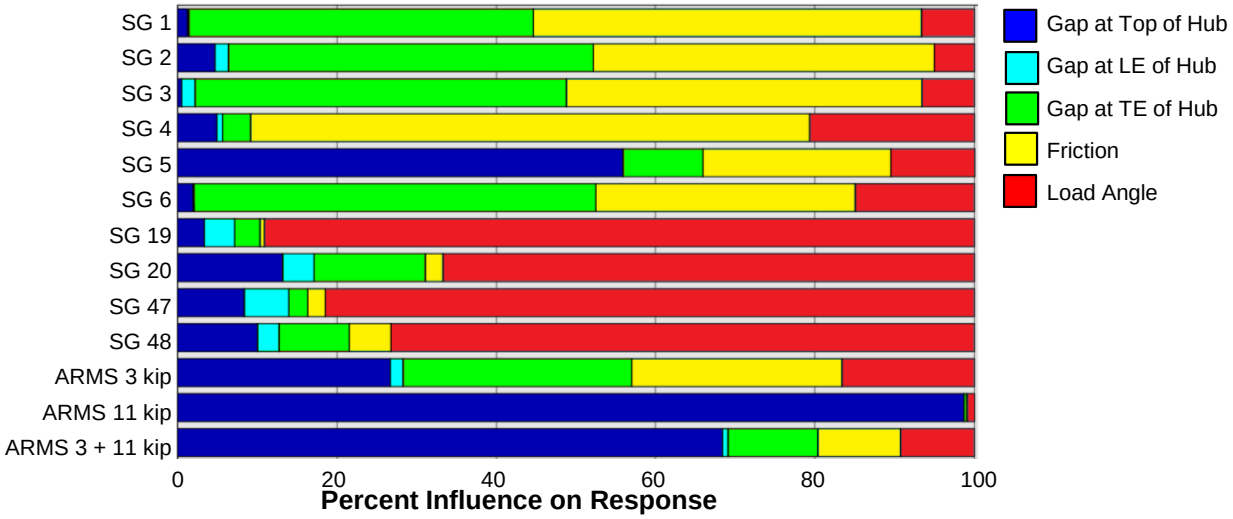

Figure 39. Global Sensitivities for Load Case 2.

C. Sensitivity of Strain Results to Aerodynamic Load Application Position and Gaps at Hub

For the optimization study in this section, four variables (gap at top of hub, gap at TE of hub, load angle, and friction at the pin) were used to minimize the computed error in the SGs. The objective function to minimize was selected as an average root means square (ARMS) error for ten SGs at two load levels (3 kips and 11 kips). ARMS error contours for this four-variable study are shown in Figure 40. During this optimization study, five iterations were performed in which the design space was reduced (centered on the optimum from the previous iteration) to improve the fit of the response surface, as illustrated by the additional trial points shown in Figures 40a and 40b. Constraints on the optimization are upper and lower limits on the gap at the top of the hup (0.0 in. to 0.10 in.), the gap at the TE of the hub (0.025 in. to 0.150 in.), load angle (-40° to -50°, based on Figure 8), and coefficient of friction (0.1 to 0.3). Based on initial response surfaces, these constraint limits were judged to be likely to bound the optimum point. The four-dimensional design space is impossible to represent graphically, so instead two-dimensional cross sections through the design space are shown. Based on initial optimization runs, the optimum load angle was determined to be at the lower bound (-50°), and this value was held constant in Figures 40a and 40b. In Figure 40a, the value of the TE hub gap was held constant (at a value of 0.0641 in.) while the top hub gap and coefficient of friction were varied. In Figure 40b, the value of the top hub gap was held constant (at a value of 0.0138 in.) while the TE hub gap and coefficient of friction were varied.

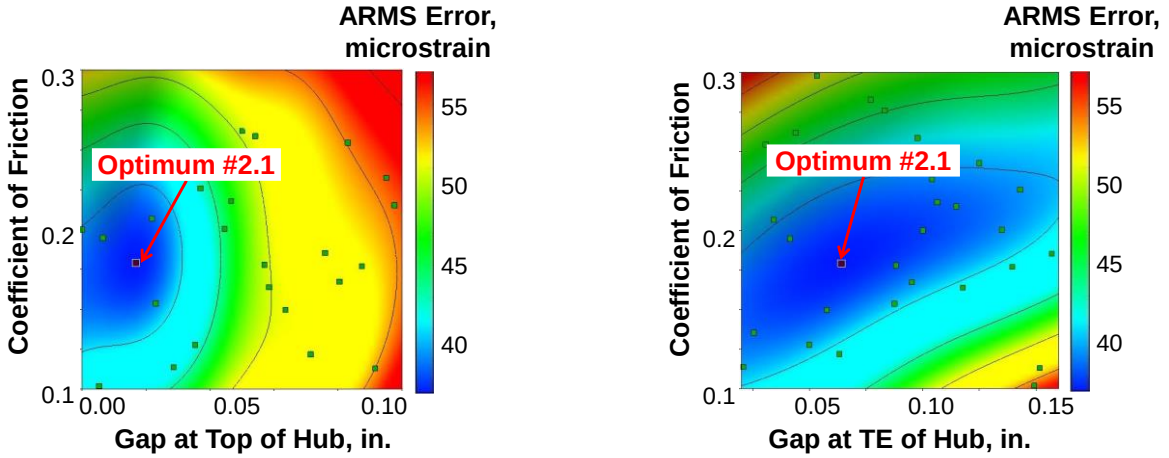

a) ARMS variation with gap at top of hub and friction (load angle = -50°, gap at TE of hub = 0.0641 in.)

b) ARMS variation with gap at TE of hub and friction (load angle = -50°, gap at top of hub = 0.0138 in.)

Figure 40. Sensitivity of ARMS error in strains to friction and gaps in the hub for load case 2.

The values for the optimum point (labeled 2.1 in Figure 40) are presented in Table 7. As shown in Table 7, the ARMS error value improved significantly. A comprehensive list of the errors in all SGs at the 11-kip load level is presented in Table 8 for both optima. In Table 8, error values less than 100 microstrain are considered good agreement and are shown in green, values between 100 and 200 microstrain are considered moderate agreement and are shown in yellow, and values greater than 200 microstrain are considered poor agreement and are shown in red. The percent error for all SGs at both optima 1.3 and 2.1 are shown in Table 9.

Table 7. Design variable and ARMS error values for optimum points 1.3 and 2.1 for load case 2.

Optimum	Hub Top Gap, in.	Hub TE Gap, in	Load Angle, deg.	Friction	ARMS at 3-kip Load, microstrain	ARMS at 11-kip Load, microstrain	ARMS at 3- and 11-kip Load, microstrain
1.3	0.0000	0.0000	-45.0	0.3000	35.42	100.15	53.11
2.1	0.0138	0.0641	-50.0	0.1877	28.75	60.84	33.64

Table 8. Error in computed SG values for optimum points 1.3 and 2.1 for load case 2.

Optimum	Error in Computed Strains at 11-kip Load, microstrain									
	Pin-Wrap Section						Airfoil Section			
	SG 1	SG 2	SG 3	SG 4	SG 5	SG 6	SG 19	SG 20	SG 47	SG 48
1.3	-379	226	594	-135	-224	-152	-33	-421	-203	-197
2.1	162	112	196	-37	-173	-82	-121	-387	-266	-162

Table 9. Percent error in computed SG values for optimum points 1.3 and 2.1 for load case 2.

Optimum	Percent Error in Computed Strains at 11-kip Load									
	Pin-Wrap Section						Airfoil Section			
	SG 1	SG 2	SG 3	SG 4	SG 5	SG 6	SG 19	SG 20	SG 47	SG 48
1.3	-84%	-72%	-101%	-64%	-31%	-208%	-2%	22%	-12%	10%
2.1	36%	-36%	-33%	-17%	-24%	-6%	-7%	20%	-16%	8%

In Table 8, SGs in pin-wrap section were in good to moderate agreement with FEA results based on error in strain values, but the percentage error seems much larger (6% to 36%) in Table 9. In Table 8, SGs in the airfoil section have a moderate to large errors in strain values, but the percent error seems smaller (7% to 20%). Because the error values and percent error values indicate different (opposite) levels of agreement for the airfoil and pin-wrap sections, to evaluate the errors in the FEA results, comparison of the SG responses at multiple load points is preferred.

Strain data from the tests [15] and from the FEA at optimum #2.1 for load case 2 are reported in Figures 41 to 44. The strain values in the airfoil section (Figure 41 and 42) follow similar trends, but the differences in strain values are large (above 200 microstrain) because the strain response is large (around 2000 microstrain). Errors in strain values in the pin-wrap section (Figures 43 and 44) followed similar trends, but the overall strain response is smaller than in the airfoil section (less than 800 microstrain, and less than 200 microstrain for several gages) so the percent error is larger.

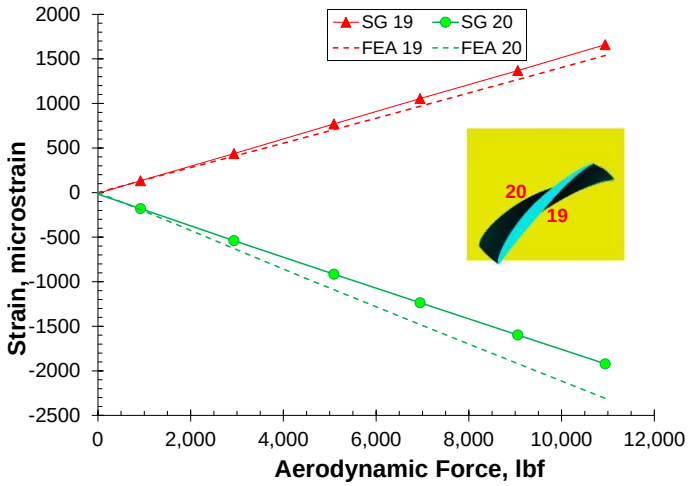

Figure 41. Strain vs. load test-analysis correlation at optimum #2.1 for load case 2 (SG 19 and 20).

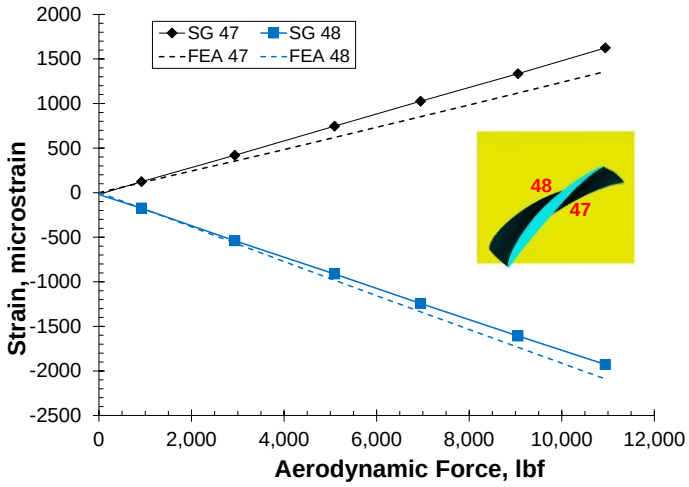

Figure 42. Strain vs. load test-analysis correlation at optimum #2.1 for load case 2 (SG 47 and 48).

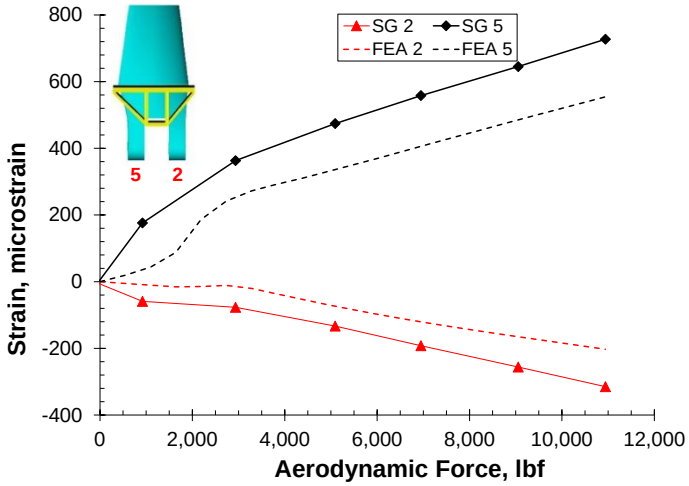

Figure 43. Strain vs. load test-analysis correlation at optimum #2.1 for load case 2 (SG 2 and 5).

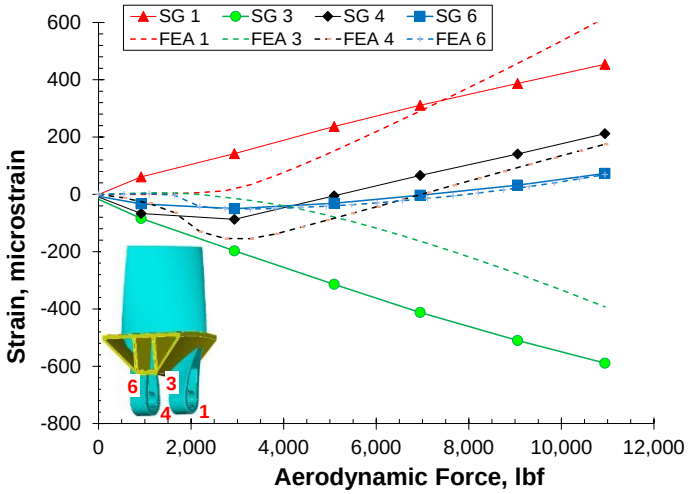

Figure 44. Strain vs. load test-analysis correlation at optimum #2.1 for load case 2 (SG 1, 3, 4, nd 6).

IX. Test-Analysis Correlation for Load Cases 3 and 6

In the report for the tests [15], no changes to the test fixtures between each load case were documented. Therefore, the test fixture parameters obtained from the optimization studies in sections VII and VIII were used in the computational model for load cases 3 and 6, and no additional optimization study was performed.

In load case 3, a combined aerodynamic and centrifugal loading was applied to mimic the 360-rpm rotation condition. During the test, the centrifugal and aerodynamic loads were simultaneously increased uniformly until 97% and 80% of maximum load, respectively. Then, both loads were increased to 100% of their respective maximum values. The test loading procedure was duplicated in the FEA as a two-step loading. Strain data from the tests and the FEA are reported in Figures 45 to 48. Again, strains in the airfoil section were mostly linear, but strains at the pin-wrap section were nonlinear. The strain values in the airfoil section (Figure 45 and 46) were within 21% of the test data, except for SG 20 with an error of 34%. Errors in strain values at the maximum load in the pin-wrap section (Figures 47 and 48) were below 41% (except SG 1 and 2 which had larger percent errors but small responses of under 200 microstrain) but the shapes of the computed and test strain curves show similar trends. Error and percent error in the individual SG data at the maximum load for load case 3 are presented in tables in the summary section.

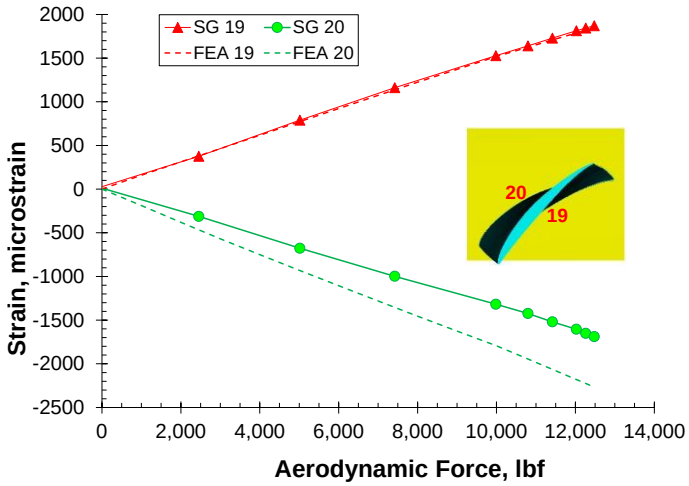

Figure 45. Strain vs. load test-analysis correlation at optimum #2.1 for load case 3 (SG 19 and 20).

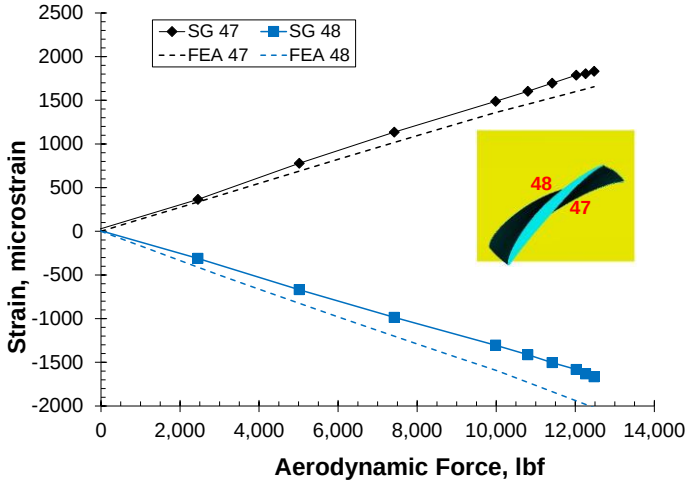

Figure 46. Strain vs. load test-analysis correlation at optimum #2.1 for load case 3 (SG 47 and 48).

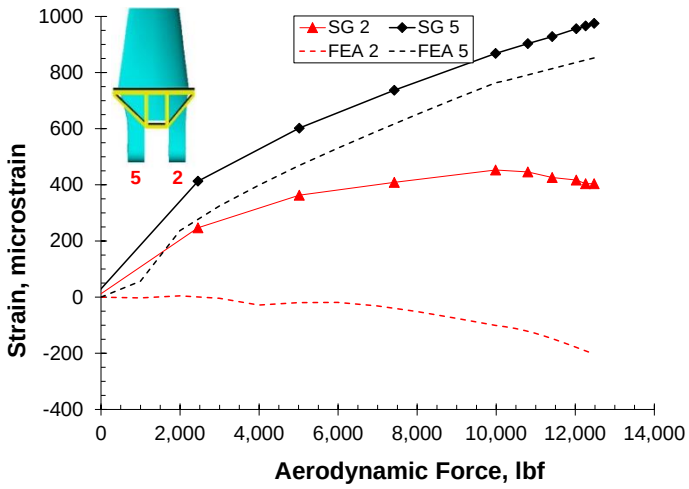

Figure 47. Strain vs. load test-analysis correlation at optimum #2.1 for load case 3 (SG 2 and 5).

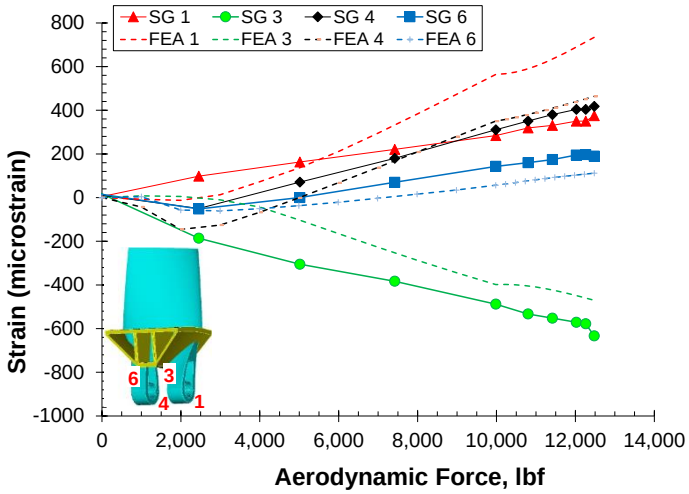

Figure 48. Strain vs. load test-analysis correlation at optimum #2.1 for load case 3 (SG 1, 3, 4, and 6).

In load case 6, a combined aerodynamic and centrifugal loading was applied to mimic the 600-rpm rotation condition. Strain data from the tests and the FEA are reported in Figures 49 to 52. During the test, the aerodynamic load was increased to 10% of its maximum value with no centrifugal load applied. Then both loads were simultaneously increased to 100% of their maximum values. The initial aerodynamic load is the reason the SG responses do not start at a value of zero. Due to the small initial aerodynamic load, the loading in the FEA simulation was done with only one step. In Figures 49 to 50, strains in the airfoil section were mostly linear, but strains at the pin-wrap sections (Figures 51 and 52) were nonlinear. The strain values in the airfoil section (Figure 49 and 50) were within 136 microstrain of the test data, except for SG 20 with an error of 313 microstrain. The percentage errors are large (108% and 71%, respectively) for SG 20 and 48 because the strain values are small (below 200 microstrain). Errors in strain values were below 182 microstrain (except SG 2) in the pin-wrap section (Figures 51 and 52) but the shapes of the computed and test strain curves are similar. As with the centrifugal load case, the error in SG 2 was much higher than the other SGs; therefore, some unpredicted mechanism must have been present in the test at that SG. Error and percent error in the individual SG data at the maximum load for load case 6 are presented in tables in section X, Summary and Discussion.

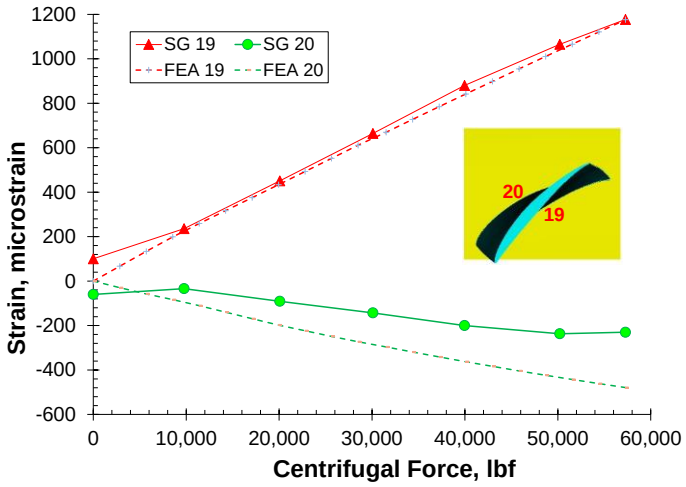

Figure 49. Strain vs. load test-analysis correlation at optimum #2.1 for load case 6 (SG 19 and 20).

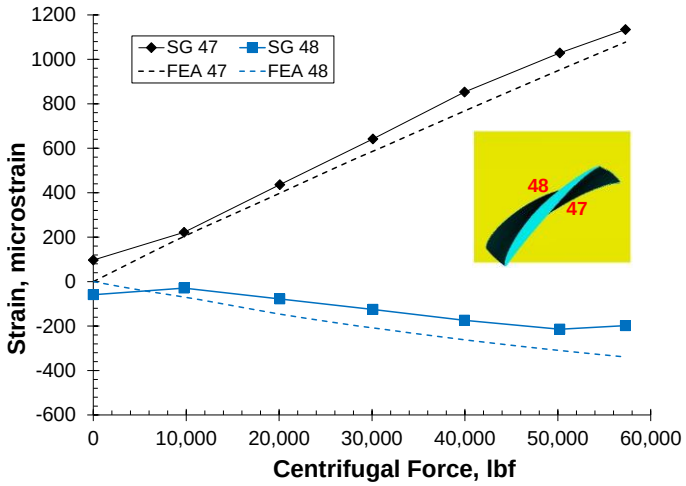

Figure 50. Strain vs. load test-analysis correlation at optimum #2.1 for load case 6 (SG 47 and 48).

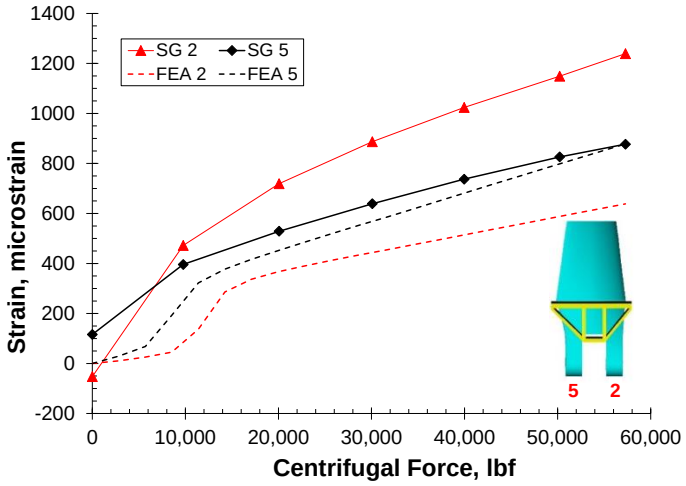

Figure 51. Strain vs. load test-analysis correlation at optimum #2.1 for load case 6 (SG 2 and 5).

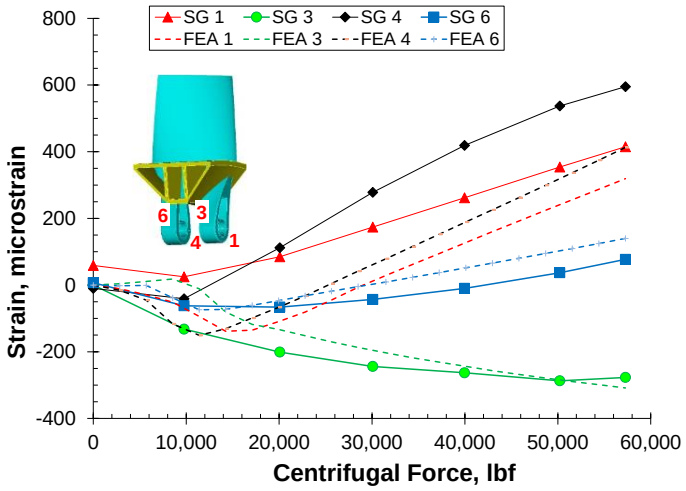

Figure 52. Strain vs. load test-analysis correlation at optimum #2.1 for load case 6 (SG 1, 3, 4, and 6).

X. Summary and Discussion

In this report, an effort to validate a structural model of a wind tunnel fan blade for the NTF against old test data was presented. First, development of CAD geometry from legacy drawings, hand measurements, and a laser scan of a physical fan blade were discussed. Next, material properties for the original fan blades and the testing procedures used to certify them were discussed. The CAD, material, and testing data were combined to create a structural finite element model of the NTF fan blade. Weight of this finite element model was within 2% of the average weight of the as-built fan blades.

The finite element model was analyzed under four loads representing conditions from static tests conducted in 1981. Test-analysis correlation was attempted in 2019, but significant differences between the test and analysis data were observed. In this current study, a formal optimization process was developed to improve the correlation. For this process, the ARMS error between test data and values computed from the finite element model was used as the objective function in the optimization. The process was set up in the LS-OPT software and utilized several of its tools including Kriging response surface evaluation, adaptive simulated annealing, and global sensitivity analysis for evaluation of design parameters. The key design parameters were unknowns in the test fixtures, which were noted during the original tests as slippage. Among these parameters were gaps between the fan blade and the pin, gaps between the fan blade and the hub, friction, loading angle, and load application position.

Four SGs used in this study were in the airfoil section (at the upper and lower surfaces), and six SGs were located in the pin-wrap section. Additional SG data was not used because those SGs could not be accurately located from sketches in the 1981 test data. A comprehensive list of the errors in all SGs at the maximum load level (centrifugal load for cases 1 and 4, aerodynamic load for cases 2 and 3) is presented in Table 10 for optimum #2.1 for all four load cases. In Table 10, error values below 100 microstrain are considered good and are shown in green, values between 100 and 200 microstrain are considered moderate agreement and are shown in yellow, and values above 200 microstrain are considered poor agreement and are shown in red.

In Table 10, good test-analysis correlation was found in the SGs in the airfoil region for load case 1. For the other load cases, correlation was good for SG 19, poor for SG 20, and variable for the other gages. The error in SGs 20 and 48 in load case 6 was on the order of the actual strain gage values (around 200 microstrain), which were low. Based on the results in Table 11, the error in the test-analysis correlation was under 12% and 20% for load cases 1 and 2, respectively. The percent error was large only for SG 20 in load case 3.

In general, moderate agreement was found between the test and analysis data in SGs 3, 4, 5, and 6 in the pin-wrap region. Test-analysis correlation for SG 1 was good under centrifugal loading but moderate to poor under aerodynamic loading. The error in SG 2 was much higher than the other SGs in the LE of the pin-wrap section. Unfortunately, the corporate knowledge associated with this test that may have explained the discrepancy in this outlier SG has been lost.

Table 10. Error in computed SG values for load cases 1, 2, 3 and 6 for optimum 2.1.

Load Case	ARMS Error for 10 SGs, microstrain	Error in Computed Strains at Maximum Load by Load Case, microstrain									
		Pin-Wrap Section						Airfoil Section			
		SG 1	SG 2	SG 3	SG 4	SG 5	SG 6	SG 19	SG 20	SG 47	SG 48
1 (Centrifugal)	78.71	-74	-761	15	-106	-129	-2	-47	-25	-70	-3
2 (Aerodynamic)	60.84	162	112	196	-37	-173	-4	-121	-387	-266	-162
3 (Maximum Aerodynamic)	97.59	359	-606	163	45	-123	-78	-22	-578	-178	-354
6 (Maximum Centrifugal)	70.24	-96	-601	-32	-182	1	63	-1	-249	-56	-141

Table 11. Percent error in computed SG values for load cases 1, 2, 3 and 6.

Load Case	Percent Error in Computed Strains at Maximum Load by Load Case									
	Pin-Wrap Section						Airfoil Section			
	SG 1	SG 2	SG 3	SG 4	SG 5	SG 6	SG 19	SG 20	SG 47	SG 48
1 (Centrifugal)	-27%	-56%	-35%	-47%	-18%	-2%	-8%	-7%	-12%	-1%
2 (Aerodynamic)	36%	-36%	-33%	-17%	-24%	-6%	-7%	20%	-16%	8%
3 (Maximum Aerodynamic)	96%	-150%	-26%	11%	-13%	-41%	-1%	34%	-10%	21%
6 (Maximum Centrifugal)	-23%	-48%	11%	-31%	0%	82%	0%	108%	-5%	71%

XI. Concluding Remarks

This study was motivated by a concern by NTF personnel that the fan blades have deteriorated over the last four decades and may need to be replaced in the next few years. Validated structural models are needed for evaluation of the current fan blades and for design of new fan blades. Unfortunately, no fan blade could be spared for destructive testing; therefore, it was necessary to use legacy static test data from 1981 for comparison against a modern finite element model.

In general, good agreement was found in the strain gages in the airfoil region. Also, moderate agreement was found in the strain gages in the pin-wrap section, although correlation of one strain gage at the leading edge wrap section was difficult. However, inclusion of the gap parameters, significantly improved the correlation and the computed curves matched the test data very well in shape if not always in magnitude. Neither the error in the strain values nor the percent error in the strain at maximum load were sufficient for test-analysis correlation, due to the small magnitudes of some strain responses. Review of the strain response with load history was necessary for a full comparison.

Due to the improved agreement with the test data compared with the previous study, this model is considered validated for use in future studies to evaluate the legacy fan blades or to design new fan blades. This study has also shown that optimization techniques can be used to improve test-analysis correlation if unknown parameters in the test fixtures are parameterized in numerical models. These techniques can be applied with limited data, and these numerical techniques are particularly useful when re-testing of results that do not agree with analytical predictions is not a valid option.

XII. Acknowledgement

The authors wish to acknowledge the technical guidance provided by Dawn C. Jegley of the Structural Mechanics and Concepts Branch. The authors also wish to acknowledge Dr. Eric Walker for his support of this activity through the AETC.

XIII. References

[1] Wahls, R. A., "The National Transonic Facility: A Research Retrospective," AIAA Paper 2001-0754, 39th AIAA Aerospace Sciences Meeting and Exhibit," January 8-11, 2001, Reno, Nevada.

[2] Grenoble, R. M., Harik, R., Munden, D. M., Halbritter, J., Jegley, D. C., and Mason, B. H., "Assessment of Automated Fiber Placement for the Fabrication of Composite Wind Tunnel Fan Blades," Proceedings of Society for the Advancement of Material and Process Engineering (SAMPE) 2019 Conference and Exhibition, Charlotte, North Carolina, May 20-23, 2019.

[3] Harik, R., Halbritter, J., Jegley, D. C., Grenoble, R. W., and Mason, B. H., "Automated Fiber Placement of Composite Wind Tunnel Fan Blades: Process Planning and Manufacturing," Proceedings of Society for the Advancement of Material and Process Engineering (SAMPE) 2019 Conference and Exhibition, Charlotte, North Carolina, May 20-23, 2019.

[4] Mason, B. H., Munden, D. M., Jegley, D. C., Grenoble, R. W., and Harik, R., "Design and Analysis of a Tool for Automated Fiber Placement of Composite Wind Tunnel Fan Blades," American Society of Composites (ASC) 34th Technical Conference, Atlanta, GA, September 23-25, 2019.

[5] Jegley, D. C., Grenoble, R. W., Mason, B. H., Harik, R., Halbritter, J., and Munden, D. M., "Hybrid AFP/Hand Layup Optimized Fan Blades to Enhance Wind Tunnel Capability: Summary of PREDICT 2018 Efforts," NASA/TM-2020-5000911, May 2020.

[6] Mason, B. H. and Lovejoy, A. E., "Structural Analysis of Wind Tunnel Fan Blades for the National Transonic Facility," AIAA 2020-0474, 61st AIAA/ASCE/AHS/ASC SDM Conference, Orlando, FL, January 6-10, 2020.

[7] Fasanella, E. L., and Robinson, M. P., "Analysis of the National Transonic Facility Mishap," NASA/TM-101686, January 1990.

[8] NASA ISAAC Fact Sheet, FS-2016-12-273-LaRC, 2021.

[9] Lovejoy, A. E., Gardner, N. W., Dawicke, D. S., Jutte, C. V., and Smith, B., "Improving Structural Test and Analysis Correlation Using Digital Image Correlation Boundary Measurements," 2020 AIAA/ASCE/AHS/ASC Structures, Structural Dynamics, and Materials Conference, AIAA Paper 2020-2188, Orlando, FL, January 6-10, 2020.

[10] Lovejoy, A. E., Jegley, D. C., Hilburger, M. W., and Przekop, A., "Lessons Learned from Large-Scale Aerospace Structural Testing," AIAA Paper 2021-1619, SciTech 2021, virtual conference, January 11-15 and 19-21, 2021.

[11] CUBIT Geometry and Mesh Generation Toolkit 15.5 User Documentation, Sandia National Laboratories, Albuquerque, NM, 87185.

[12] https://industry.nikon.com/en-gb/case-studies/laser-scanning-the-powerful-flexible-tool-of-choice-for-advanced-manufacturing/.

[13] https://www.creaform3d.com/en/metrology-solutions/products/optical-measuring-systems/technical-specifications-maxshot-3d.

[14] Kilch, P. J., Richards, W. H., and Ahl, Jr., E. L., "National Transonic Facility Fan Blade Prepreg Material Characterization Tests," NASA-TM-81800, July 1981.

[15] Kilch, P. J., and Stalnaker, W. A., "Summary of NTF Prototype Fan Blade Static Load and Fatigue Test Data and Test Procedures," December 3, 1981.

[16] Kilch, P. J., "Summary of NTF Prototype Fan blade Centrifugal Force (C_F) Test Data and Test Procedures," June 10, 1981.

[17] Friedman, I. P., "Weight, Center of Gravity, and Modal Test Report for NTF Fan blade Set No. 3," NASA Contractor Report 189583, Dynamic Engineering Incorporated, Newport News, VA, February 1992.

[18] Hunter, W. F., Boxer, E., "NTF Fan Blade Analysis Work Package No. 11.2: Section IV Aerodynamic Loads," March 15, 1982.

[19] PATRAN 2016 Release Guide, MSC Software, MSC Software, Santa Ana, CA 92707.

[20] ABAQUS, ABAQUS User's Manual, Vol III, Version 6.12, Dassault Systèmes Simulia Corp., Pawtucket, RI, 2012.

[21] Stander, N., Eggleston, T., Craig, K, and Roux, W., "LS-OPT User's Manual A Design Optimization and Probabilistic Analysis Tool for the Engineering Analyst," Version 2, Oct. 2003.

[22] Tang, B., "Orthogonal Array-Based Latin Hypercubes," *Journal of the American Statistical Association*, Vol. 88, No. 424, pp. 1392-1397, 1993.

[23] Koehler, J. R. and Owen, A. B., "Computer Experiments," *Handbook of Statistics*, Elsevier Science, New York, 1996, pp. 261-308.

[24] Sobol, I.M., Tarantola, S., Gatelli, D., Kucherenko, S.S, and Mauntz, W., "Estimating Approximation Error When Fixing Unessential Factors in Global Sensitivity Analysis," *Reliability Engineering and System Safety 92* (2007) pp. 957-960, © 2006 Elsevier LTD.

[25] Horta, Lucas G., Mason, Brian H., and Lyle, Karen H., "A Computational Approach for Probabilistic Analysis of Water Impact Simulations," *International Journal of Crashworthiness*, Vol. 5, No. 6, December 2010, pp. 649-665.